MEASURING SNOW AND GLACIER ICE PROPERTIES FROM SATELLITE

Max König,
Jan-Gunnar Winther,
and Elisabeth Isaksson
Norwegian Polar Institute
Polar Environmental Centre
Tromsø, Norway

Abstract. Satellite remote sensing is a convenient tool for studying snow and glacier ice, allowing us to conduct research over large and otherwise inaccessible areas. This paper reviews various methods for measuring snow and glacier ice properties with satellite remote sensing. These methods have been improving with the use of new satellite sensors, like the synthetic aperture radar (SAR) during the last decade, leading to the development of new and powerful methods, such as SAR interferometry for glacier velocity, digital elevation model generation of ice sheets, or snow cover mapping. Some methods still try to overcome the limitations of present sensors, but future satellites will have much increased capability, for example, the ability to measure the whole optical spectrum or SAR sensors with multiple polarization or frequencies. Among the methods presented are the satellite-derived determination of surface albedo, snow extent, snow volume, snow grain size, surface temperature, glacier facies, glacier velocities, glacier extent, and ice sheet topography. In this review, emphasis is put on the principles and theory of each satellite remote sensing method. An extensive list of references, with an emphasis on studies from the 1990s, allows the reader to delve into specific topics.

1. INTRODUCTION

There have been tremendous technological achievements in the twentieth century that enable scientists to undertake research at virtually every spot on Earth. In parallel, advances in space technology during the last decades have provided us with a rapidly increasing number of satellite platforms that can be used to study complex physical processes of the Earth-atmosphere system. The development within this field concerns not only the growing number of satellites but also the rapid progression of sensor capabilities. In the future a major challenge will be connected with combining various sources of information gathered from space, i.e., data assimilation, and to make use of this information in a systematic, repetitive manner to monitor temporal and spatial variability, for example, in climate-change research.

In the field of glaciology, satellite remote sensing has proven to be a particularly useful tool because areas of interest are often inaccessible. Further, in many regions at high latitudes, like the Greenland and Antarctic ice sheets, it is only during parts of the year that effective ground-based research can be carried out due to the harsh climate environment and the lack of daylight. Satellite remote sensing often permits real-time, year-round, and long-term studies. Also, the large spatial coverage of satellite remotely sensed data enables monitoring and process studies over large areas. In this way, satellite data help in understanding processes and teleconnections on the regional, continental, or even global scale, for example, global satellite-derived maps of snow cover. Such products are particularly important because they assist interpretation and analysis concerning global change.

Also, on smaller scales, satellite remote sensing can be a vital tool both for obtaining a basic understanding of processes (e.g., glacier velocities from interferometry products) and for monitoring programs (e.g., glacier retreat for climate change detection). Monitoring or routine measurements can also provide early warnings (e.g., disintegration of ice shelves at the Antarctic Peninsula) or even surprises. One illustrative example of the latter is the satellite-derived detection of a large iceberg break-off from the Filchner-Ronne ice shelf in Antarctica in October 1998: A German summer station, the Filchner Station, happened to be located on this particular iceberg. On the basis of information from space, the German Antarctic Program was able to take necessary precautions before the upcoming Antarctic season.

Previous reviews on remote sensing of snow and glacier ice have been done by *Hall and Martinec* [1985], *Foster et al.* [1987], *Rott* [1987], *Bernier* [1987], and *Massom* [1991]. For complementary information we also want to refer to *Bindschadler* [1998] for satellite studies
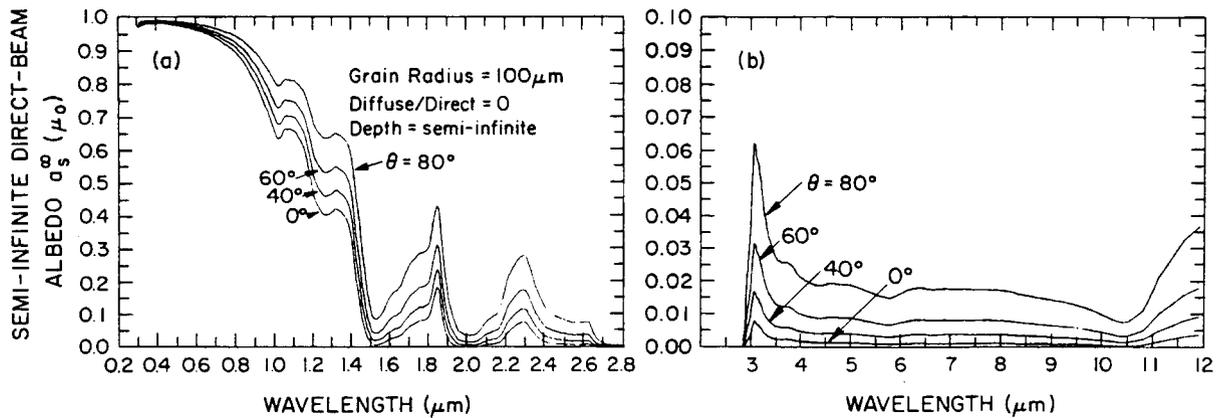
Figure 1. Semi-infinite direct-beam albedo versus wavelength for several values of direct-beam zenith angles. Reprinted from *Wiscombe and Warren* [1980] with permission from the American Meteorological Society.

of ice sheets. A thorough overview on existing satellite sensors is given by *Massom* [1995]. Building upon these studies, this paper reviews various methods for measuring snow and glacier ice properties with satellite remote sensing. Emphasis is especially put on explaining the principles and theory of each method. An extensive list of references, with an emphasis on studies from the 1990s, allows the reader to delve into specific topics. We have tried to identify the most important studies within each field, but because of the large number of articles published we are aware that our review cannot be complete and that some work or topics may be missing. We excluded, for example, ground studies and most studies using airborne remote sensing.

2. REMOTE SENSING OF SNOW

Snow plays an important role in the Earth's climate system. A snow cover insulates the ground, and fresh snow reflects up to 80% or more of the incoming solar energy, which compares drastically with only 20% or less for bare ground [*Weller and Holmgren*, 1974]. In Arctic regions, such a change of reflectance can take place within only a few days during spring snowmelt. The global extent of snow therefore has great influence on the Earth's climate and biota. Extent and snow volume in terms of depth and snow water equivalent (SWE) are important for runoff assessment, water management, and flood control. Fifty to ninety percent of the annual precipitation and runoff in Arctic regions is from snowfall [*McNamara et al.*, 1998; *Winther and Hall*, 1999]. The study of albedo, snow grain size, and surface temperature is applicable not only to snow cover on land, but also to snow cover on glaciers and ice sheets and can therefore also be viewed as remote sensing of glaciers. These properties are often also important input parameters for various models, such as surface runoff and energy balance models.

2.1. Reflectance and Albedo

2.1.1. Reflectance characteristics and factors influencing reflectance.
The spectral region between 0.4 and 3 μm is called the reflective part of the spectrum, because reflection is the predominant mechanism, whereas emission predominates in the thermal infrared region (3–100 μm). The measured property for wavelengths below 3 μm therefore is reflectance, being the percentage of energy reflected at wavelength λ. Reflectance varies strongly with λ (Figure 1), and the resulting reflectance curve, i.e., reflectance versus λ, is unique for each surface type (Figure 2). This allows us to identify various surface types and differentiate them from each other. Albedo is then reflectance integrated over the reflective part of the spectrum.

Present satellite sensors only measure reflectance for a limited number of wavelength bands $\Delta\lambda$. The Landsat thematic mapper (TM), for example, has six bands between 0.4 and 3 μm and measures therefore only six limited parts of the reflectance curve in Figure 1. The sensor may thus be unable to differentiate surfaces having similar reflectance in these wavelength bands. An example is the difficult differentiation between snow and clouds discussed below (see section 2.3.1). For albedo determination the limited number of bands means a discontinuous coverage of the spectrum. Thus additional information is needed for wavelengths not covered by a wavelength band (see section 2.1.2). The new generation of satellite sensors, however, will eventually eliminate these problems.

The Moderate-Resolution Imaging Spectroradiometer (MODIS) and the Medium-Resolution Imaging Spectrometer (MERIS) belong to a new class of satellite sensors with greatly improved capabilities (Table 1). These imaging spectrometers are able to record a continuous spectral range, in contrast to multispectral scanners, as, for example, Landsat or Système Probatoire Pour l'Observation de la Terre (SPOT), which only
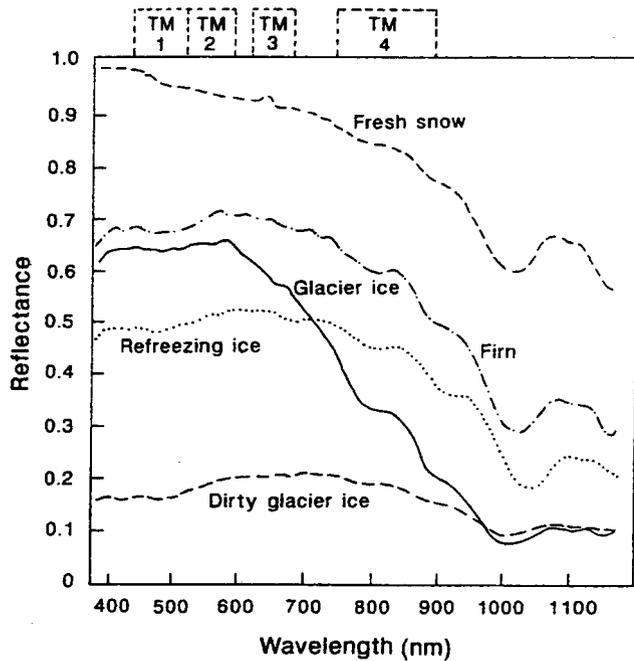
Figure 2. Spectral reflectance curves for snow and ice in different formation stages (modified from *Zeng et al.* [1984]). Reprinted with permission from the International Association of Hydrological Sciences.

record distinct, selected bands within a spectral region. MERIS and MODIS will have 15 and 36 selected bands in their spectral range, but future satellite sensors will provide real continuous coverage and allow whole spectral curves to be recorded. The Airborne Visible and Infrared Imaging Spectrometer (AVIRIS), which is not part of this review, is such an example. The Earth Observer 1 (EO 1), launched in November 2000, has an imaging spectrometer called Hyperion. Hyperion has 220 bands, giving continuous coverage between 400 and 2500 nm in 10-nm intervals. It will work, however, only on an experimental basis.

Important studies on the reflective properties of snow were done by *Wiscombe and Warren* [1980], *Warren and Wiscombe* [1980], *Warren* [1982], and *Zeng et al.* [1984], and a summary on factors influencing reflectance is given by *Foster et al.* [1987], *Winther and Hall* [1999], and *Winther et al.* [1999]. Impurities in the snow cover like carbon soot, volcanic ash, and continental dust have a strong effect on reflectance, but mostly in the visible region (0.4–0.7 μm). Grain size affects reflectance mostly in the near and middle infrared (0.7–3.0 μm), leading to lower reflectance for larger grain sizes (Figure 3). Satellite bands in this region have therefore been used for grain size determination [see, for example, *Dozier et al.*, 1981; *Bourdelles and Fily*, 1993; *Fily et al.*, 1997, 1999]. Liquid water content in the snowpack has the effect of increasing the effective grain size and thus of lowering the albedo. Model work by *Choudhury and Chang* [1979], *Wiscombe and Warren* [1980], and *Warren* [1982] furthermore concludes that snow reflectance is

independent of snow density. Observed density dependence may therefore actually be a dependence on grain size [*Warren*, 1982].

Reflectance of snow is anisotropic and dependent on incidence and view angle. This dependence is described by the bidirectional reflectance function (BDRF). *Knap and Reijmer* [1998], for example, have examined the BDRF for wavelengths equivalent to Landsat TM bands 2 and 4 and find errors of several percent when neglecting the BDRF. However, most satellite-derived albedo studies have generally not corrected for the anisotropic reflectance behavior of snow. The effect of anisotropic reflection increases as snow metamorphoses, for example, with increasing grain size and surface melt-freeze processes that sometimes produce a highly specular surface ("firnspiegel").

2.1.2. Measuring reflectance and albedo from satellite. The following method uses the Landsat thematic mapper (TM) and has been widely used for determining albedo from space [*Dozier*, 1984, 1989; *Hall et al.*, 1989, 1990a, 1990b, 1992a; *Winther*, 1992; *Winther and Hall*, 1999]. First, the raw digital numbers (DN) of the image are converted to spectral radiance L_λ, i.e., reflected energy. L_λ for DN = 0 and DN = 255 is known from satellite characteristics, and L_λ for the remaining digital numbers is calculated by linear interpolation [*Markham and Barker*, 1986]. It follows that

at-satellite planetary reflectance ρ_p

$$= \frac{\text{reflected energy } L_\lambda}{\text{incoming solar energy } E_s}. \quad (1)$$

Ground reflectance deviates from ρ_p due to gaseous absorption and scattering by molecules and aerosols in the atmosphere [*Tanré et al.*, 1990]. *Hall et al.* [1989] reported ground reflectance to be 5–17% higher than Landsat at-satellite reflectance over the Forbindels glacier in Greenland. In order to get ground reflectance, at-satellite reflectance ρ_p needs to be corrected for atmospheric effects with radiative transfer models (e.g., using the computer code by *Tanré et al.* [1990]).

The ground reflectance calculated so far is only the narrowband reflectance of a particular spectral band of wavelength $\Delta\lambda$. Albedo, however, is defined as the reflectance integrated over the visible to infrared regions of the spectrum (0.4–3 μm). Narrowband reflectance $\rho_{\Delta\lambda}$ is the percentage of energy reflected in $\Delta\lambda$. For the same interval $\Delta\lambda$, the incoming solar energy is $E_{s\Delta\lambda}$. The reflected energy is thus $E_{s\Delta\lambda}\rho_{\Delta\lambda}$. It follows that $\Sigma E_{s\Delta\lambda}\rho_{\Delta\lambda}$ is the integrated reflected energy and $\Sigma E_{s\Delta\lambda}$ is integrated incoming energy. Albedo a is thus

$a =$ integrated reflectance

$$= \frac{\text{integrated reflected energy}}{\text{integrated incoming energy}} = \frac{\displaystyle\sum_{\Delta\lambda} E_{s\Delta\lambda}\rho_{\Delta\lambda}}{\displaystyle\sum_{\Delta\lambda} E_{s\Delta\lambda}}.$$

$$(2)$$

TABLE 1. Comparison of Sensors in the Visible and Infrared Spectrum

	MERIS (Envisat)	MODIS (Terra)	MOS (IRS/(PRIR))	TM (Landsat 4–5)	ETM+ (Landsat 7)	MSS (Landsat 1–7)	HRV (SPOT 1–5)	ASTER (Terra)	AVHRR 1–3 (NOAA 9–15)	AATSR (Envisat)	ATSR-2(1) (ERS-1/2)
Type	CCD push broom scanner	CCD whisk broom scanner	CCD push broom scanner	Optomechanical scanner	Optomechanical scanner	Optomechanical scanner	CCD push broom scanner	Optomechanical scanner	Optomechanical scanner	Optomechanical scanner	Optomechanical scanner
Pixel size, m (bands)	300 (1–15) 1200 (1–15)	250 (1, 2) 500 (3–7) 1000 (8–36)	520	30/120 (6)	30/60 (6) (15 PAN)	79	10 (Pan) 20 (1–3)	15 (1–3) 30 (4–9) 90 (10–14)	1100 (1–5) 4000 (1–5)	1000	1000
Spectral range, nm	390–1040	405–14,385	403–1650	450–12,500	450–12,500	500–1100	500–890 (1750)	520–11,650	580–12,400	550–12,000	500 (1600)–12,000
Number of bands	15	36	18	7	7 + PAN	4	3 (4 on SPOT 4) + PAN	14	4/5/6	7	7 (4)
Temporal resolution, days	<3	<3	<5	<16	<16	<16/18	<3	<16	0.5	3	3
Revisit, days	35	16	5	16	16	16/18	26	16	1	35	35
Size of image, km	296 × 296 575 × 575 low resolution: 1150 × 1150	2330 × 2020	200 × 200	185 × 172	185 × 170	185 × 185	60 × 60	60 × 60	2800 × various	512 × 512	512 × 512
Swath, km	1150	2330	200	185	185	185	60	60	2800	512	512
Ground coverage	up to 86.6°	up to 90°	Europe, North America (east), India	up to 81°	up to 81°	up to 81°	up to 80°	up to 85° (1–9) up to 83° (10–14)	up to 90°	up to 83.9°	up to 83.9°
Mission date	June 2001	Dec. 1999	March 1996	July 1982 to July 1987; March 1985	April 1999	since 1972	Feb. 1986; Jan. 1990; Sept. 1993; March 1998; 2002	July 1999	since 1978	May 2000	July 1991
Altitude, km	799.8	705	817	705	705	910/705	830	705	833	799.8	785
Inclination	98.55°	98.3°	98.7°	98.2°	98.2°	99.2°/98.2°	98.8°	98.3°	98.8°	98.55°	97.5°

Platform is given below sensor, in parens.
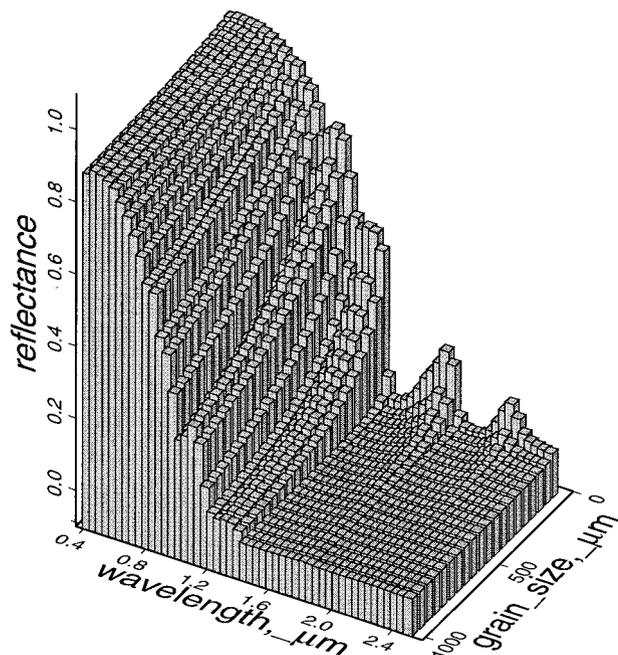
Figure 3. Spectral reflectance of snow from 0.4 to 2.5 μm as a function of grain size [from *Nolin and Dozier*, 1993]. Note the steep decrease in reflectance with increasing grain size in the spectral region between 0.7 and 1.3 μm. Calculations were made using a discrete-ordinate radiative transfer model. Reprinted from *Remote Sensing of the Environment* with permission from Elsevier Science.

Here we encounter the problem that we need to integrate over the whole spectrum. This will be possible with imaging spectrometers, as discussed earlier. For present sensors like Landsat, however, reflectance is only known in the regions Δλ covered by Landsat's spectral bands. To fill these gaps, *Hall et al.* [1989] interpolated reflectances in the visible region, where variation is low. Modeled values from *Choudhury and Chang* [1979] have been used between 0.9 and 3 μm. It is important to use the full spectrum for calculating albedo since the reflectance of snow drops to very low values in the shortwave infrared [*Hall et al.*, 1989]. Assuming that visible reflectance represents surface albedo results in albedo values that are too high.

More accurately, albedo is hemispheric reflectance integrated over all incidence angles. The satellite, however, measures only reflectance in the look direction, assuming the reflectance for other incidence angles to be the same as the measured reflectance. This method thus is correct only for a surface that is 100% reflective and diffuse (Lambertian reflector), reflecting incoming energy equally in any direction. However, in reality, snow reflects anisotropically due to its bidirectional reflectance characteristics described by the BDRF, as discussed above, and a specular, forward scattering component increases with age of the snow (i.e., the snow grain size) and low Sun angle [*Wiscombe and Warren*, 1980]. The method above therefore may overestimate or un-

derestimate albedo slightly due to this increased forward scattering [*Hall et al.*, 1989]. *Hall et al.* [1990b] find that in situ and Landsat-derived albedo values correspond within 6% in the Wrangell Mountains in Alaska.

An alternative method for converting narrowband reflectance to albedo is to use an empirical relation instead of using (2). These equations connect the values of the narrowband reflectance of the different sensor bands ($\rho_{\Delta\lambda(1)}$ and $\rho_{\Delta\lambda(2)}$, e.g., TM2 and TM4) to albedo a with constants c_1 through c_4, as in the following example taken from *Knap et al.* [1999]:

$$\text{albedo } a = c_1\rho_{\Delta\lambda(1)} + c_2(\rho_{\Delta\lambda(1)})^2 + c_3(\rho_{\Delta\lambda(2)}) + c_4(\rho_{\Delta\lambda(2)})^2. \tag{3}$$

Knap et al. [1999] compare such weighting functions with ground measurements on Morteratsch glacier, Switzerland. These relations frequently give poor agreement with ground measurements at places other than those for which they were developed. Additionally, some of these relations are only designed for specific surface types, like snow, clean ice, or dirty ice, and require prior classification.

The advanced very high resolution radiometer (AVHRR) has also been used for determining snow albedo. Use of the AVHRR, with its 1100-m resolution, is acceptable for large ice sheets, like Greenland, where large areas of similar snow conditions exist. On smaller ice masses and over seasonally snow covered ground, mixed pixels occur frequently, containing several surface types within one pixel, which makes interpretation difficult.

The method for determining albedo with AVHRR is principally the same as described for Landsat data. *Haefliger et al.* [1993], *Knap and Oerlemans* [1996], and *Stroeve et al.* [1997] calculate narrowband ground reflectance on the Greenland ice sheet with AVHRR. Differences to ground measurements (overestimation or underestimation) are generally between 2 and 14%. Both *Knap and Oerlemans* [1996] and *Stroeve et al.* [1997] find that errors due to atmospheric correction or anisotropic reflection are too small to account for this deviation, and all three studies assume sensor drift and inaccurate calibration constants to be the main cause of error. *Knap and Oerlemans* [1996] also calculate albedo from narrowband reflectance using a weighting function given by *Li and Leighton* [1992], comparable to (3). The difference compared with ground measurements here is ~8%. *Stroeve et al.* [1997] conclude in their study that *Li and Leighton*'s [1992] weighting function is insufficient for calculating snow albedo because atmospheric correction is applied after integrating at-satellite, narrowband reflectance. Calculating ground albedo from integrated at-satellite reflectance assumes equal atmospheric attenuation for all wavelengths. Atmospheric attenuation, however, varies with wavelength, and narrowband reflectance needs to be atmospherically corrected before conversion to integrated reflectance.

2.2. Surface Temperature

Emission of radiation is the dominating effect in the thermal infrared region (3–100 μm). Satellite sensors have their thermal infrared bands located between 10.5 and 12.5 μm. In this region, atmospheric effects are minimal. Additionally, even though infrared emission varies with wavelength, the emissivity is close to 1.0 for the wavelengths between 10.5 and 12.5 μm [*Warren*, 1982; *Dozier and Warren*, 1982]. Therefore the assumption is generally made that the snow surface approximates a blackbody in this part of the spectrum. It absorbs incoming energy in this wavelength region and radiates it according to surface temperature. *Dozier and Warren* [1982] show that emissivity is dependent on viewing angle and that neglecting to account for this fact can lead to errors of up to 3 K.

Orheim and Lucchitta [1988] see surface patterns in Antarctic snow in TM band 5 (1550–1750 nm) and TM band 7 (2080–2350 nm) due to grain size dependence that do not appear in the thermal infrared TM band 6. This suggests that the emissivity is insensitive to snowpack parameters in TM band 6 (10.4–12.5 μm), which also is shown by modeling [*Wiscombe and Warren*, 1980]. This wavelength region can thus be used for calculating surface temperature. *Salisbury et al.* [1994], however, find that emissivity does vary due to particle size, density, and liquid water content in this wavelength region. This departure from blackbody behavior can lead to errors. Some examples of surface temperature determination are given in the following:

Landsat TM band 6 has been used for surface temperature calculation by *Orheim and Lucchitta* [1988], *Pattyn and Decleir* [1993], and *Winther* [1993a]. Comparison with ground measurements shows quite large deviations, usually an overestimation or underestimation of ~10°C. Inaccurate prelaunch and atmospheric effects have been assumed to be the reasons. Both *Orheim and Lucchitta* [1988] and *Pattyn and Decleir* [1993] conclude that Landsat TM band 6 "faithfully" reproduced relative temperature variations but not absolute temperature.

Key and Haefliger [1992] developed an algorithm for surface temperature retrieval, it principally being a weighting function comparable to (3) for albedo, which relates brightness temperature from AVHRR bands 4 and 5 (10.3–11.3 μm and 11.5–12.5 μm) to surface temperature. A short summary of the method is given by *Haefliger et al.* [1993]. The accuracy has been determined to be between 1 and 4 K [*Key et al.*, 1997]. A refined version, presented by *Key et al.* [1997] for AVHRR and the Along Track Scanning Radiometer (ATSR), finds an agreement with ground measurements between 0.3 and 2.1 K, where the larger errors are attributed to spatial variation within the low-resolution pixel. *Bamber and Harris* [1994] and *Stroeve et al.* [1996], using the dual-angle view of ATSR, report an accuracy of better than 0.2 K for their algorithms. ATSR looks at the surface both vertically and inclined in the forward direction, which allows much improved atmospheric correction with increased accuracy.

2.3. Snow Extent, Snow-Covered Area (SCA)

2.3.1. Small-scale mapping.
An automated snow-mapping algorithm was presented by *Dozier* [1989]. A threshold in Landsat TM band 1 (450–520 nm) differentiates snow and clouds from other surfaces, while a threshold in TM band 5 (1550–1750 nm) differentiates snow and clouds. As an additional requirement, the normalized difference image between TM band 2 (520–600 nm) and TM band 5 distinguishes snow from bright soils, rocks, and clouds. Using this algorithm, a pixel is identified as either snow-covered or non-snow-covered. This introduces an error for mixed pixels. Spectral mixture analysis has been used to overcome this problem [*Nolin et al.*, 1993; *Rosenthal and Dozier*, 1996]. The spectrum of a single pixel, i.e., reflectance values plotted against the wavelength or sensor band, is a mixture of the spectra of the different surfaces contained within the pixel. Spectral mixture analysis models the pixel spectrum with a least squares fit as a linear combination of the different surface spectra that are present within the pixel. The surface spectra are thus extracted, and the fractional contribution of each surface spectrum to the pixel spectrum is determined. Assuming that this fractional contribution equals aerial fraction of that surface, an image can now be displayed showing fractional snow coverage of each pixel [*Nolin et al.*, 1993].

Pixel reflectance usually needs to be corrected for topographic effects with a digital elevation map (DEM) when illumination varies due to slope, aspect, and shaded areas. Spectral mixture analysis correctly identifies surfaces without topographic correction if the spectra for different illumination differ only in amplitude but not in shape [*Rosenthal and Dozier*, 1996]. To allow operational snow mapping, *Rosenthal and Dozier* [1996] identify fractional snow cover in the Sierra Nevada with spectral mixture analysis for only a few representative regions. They then use a faster decision tree to identify pixels with the same fractional snow cover on larger areas. By testing against aerial photography and ground data, *Rosenthal and Dozier* [1996] conclude that this method gives results as accurate as, but faster and less expensive than, snow mapping with high-resolution photography. However, this method has yet been proven to work in an automated way over large areas (e.g., globally), and present operational algorithms do not use this method.

The occurrence of mixed pixels is a general problem in snow mapping and makes a pixel's assignment to a particular surface type difficult. The larger the pixel size is, the larger the likelihood is that a pixel contains several surface types. Erroneous assignments of a single pixel thus result in a larger aerial error for larger pixel sizes. Figure 4 shows the same area mapped with Landsat TM (30-m pixel), AVHRR (1100-m pixel), and Spe-
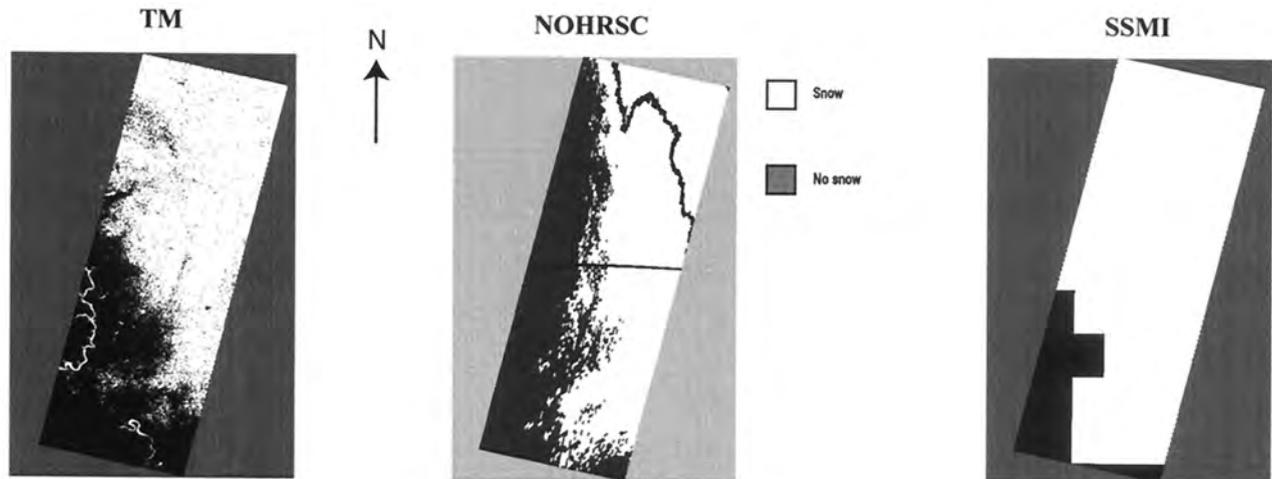
Figure 4. North and South Dakota, United States. (left) Landsat thematic mapper (TM) derived snow map acquired on February 7, 1998, using the Moderate-Resolution Imaging Spectroradiometer (MODIS) SNOW-MAP algorithm. (middle) National Operational Hydrologic Remote Sensing Center (NOHRSC) snow map acquired on February 7, 1998. (right) Special Sensor Microwave Imager (SSM/I) derived map from February 7–8, 1998, using the algorithm from *Chang et al*. [1987]. Each image is 185 km across. [After *Hall et al*., 2000].

cial Sensor Microwave Imager (SSM/I) (25-km pixel). Differences are obvious and due to scale as well as to differences in methods. Errors in snow mapping due to scale effects have not yet been reported in detail. Even though the problem of mixed pixels is smaller for high-resolution sensors like Landsat or synthetic aperture radar (SAR), these sensors are not being used for regular, operational snow mapping. The reason is the low temporal resolution, being at most two times per month (see Tables 1 and 2), whereas sensors with lower resolution provide daily images of the same area. A good compromise is MODIS, described further below, with its pixel size of 500 m and almost daily repeat time.

A general limitation for accurate snow mapping in the visible part of the spectrum is the presence of cloud cover, which can hinder mapping of snow for long peri-

TABLE 2. Comparison of Synthetic Aperture Radar and Passive Microwave Sensors

	ASAR (Envisat)	*AMISAR (ERS-1/ERS-2)*	*SAR (RADARSAT)*	*SAR (JERS 1)*	*SIR-C (Space Shuttle)*	*X-SAR (Space Shuttle)*	*SSM/I (DMSP F8, F10, F11–14)*	*SMMR (Nimbus 7)*
Band	C	C	C	L	C, L	X	⋯	⋯
Frequency, GHz	5.3	5.3	5.3	1.275	5.3/1.275	9.6	19.35, 22.235, 37.0, 85.5	6.6, 10.7, 18.0, 21.0, 37.0
Polarization	HH/VV	VV	HH	HH	HH, VV, HV, VH	VV	V (all), H (not 22.2)	V, H
Resolution, m	<30/150/1000	<30	8–100	18	25	10–25	>25,000	>25,000
Repeat, days	35	35	24	44	N/A	N/A	<1	<6
Incidence angle	14°–45°	20°–26°	10°–60°	37°–43°	20°–55°	15°–55°	53.1°	50.3°
Image size, km	100 × 100 400 × 400	100 × 100	50 × 50 to 500 × 500	75 × 80	100 × 62.5	100 × 62.5 50 × 31.2	⋯	⋯
Swath, km	60–100 400	100	45–500	75	10–100	50/100	1400	780
Coverage	up to 87.5°N, 79.8°S	up to 84.5°	up to 90°	up to 85.5°	up to 60° (selected areas)	up to 60° (selected areas)	up to 90°	up to 85°
Mission	launch June 2001	since July 17, 1991/ since April 20, 1995	since Nov. 4, 1995	Feb. 11, 1992	April and Oct. 1994; Sept. 1999	April and Oct. 1994; Sept. 1999	since July 1987	Oct. 1978 to Aug. 1987
Altitude, km	799.8	785	798	568	222	222	830	955
Inclination	98.55°	97.5°	98.7°	97.7°	57°	57°	98.8°	99.1°

Satellite is given below sensor, in parens.

ods of time, thus lowering the temporal resolution of optical sensors even further. On partly cloudy images it can be impossible to distinguish snow from clouds, since both have a similar reflectance up to 1100 nm [*Massom*, 1991]. Between 1.55 and 1.75 μm, however, snow reflectance drops to almost zero, while reflectance of most clouds remains high. Thus a spectral band in this region (e.g., Landsat TM band 5 for small-scale mapping, MODIS band 6 and AVHRR-3 band 3a for medium-scale mapping) allows snow/cloud discrimination, detecting cirrus, stratus, and cumulus clouds. Thin cirrus clouds, however, are often not discriminated from snow with this method [*Hall et al.*, 1995a].

SAR presently allows only limited snow mapping. Like passive microwave remote sensing, discussed below, SAR enables mapping through cloud cover. Being an active sensor, the resolution is about 3 orders of magnitude higher than with passive microwave sensing (tens of meters versus tens of kilometers). The interpretation of the recorded backscatter σ, however, is more complicated. At SAR wavelengths the radar penetration depth is of the order of 20 m for cold and dry snow [*Rott and Nagler*, 1994], the major scattering source being the snow-ground interface. This makes it hardly possible to separate dry snow from bare ground, at least with single-polarization, single-frequency SAR [*Rott and Nagler*, 1994; *Koskinen et al.*, 1997]. Just a small amount of liquid water, however, reduces the penetration depth to a few centimeters, making surface scattering more dominant than volume scattering. *Rott and Nagler* [1993] find a penetration depth of 13.8 cm for 1% liquid water content and 4.9 cm for 3% (compared with 20 m for dry snow). It is therefore possible to map wet snow cover. However, wet snow and wet soil [*Haefner et al.*, 1994] or wet snow and smooth surfaces [*Shi and Dozier*, 1997] can still be indistinguishable. *Guneriussen* [1998] find that snow and bare ground on Kongsfjellet, Norway, can be better discriminated at high incidence angles. RADARSAT and Envisat advanced SAR (ASAR), having higher incidence angles than ERS SAR, are therefore expected to give better results.

Very accurate radiometric and geometric corrections are necessary when using a single SAR image, requiring high-resolution DEMs [*Guneriussen et al.*, 1996]. *Rott and Nagler* [1994] use multitemporal images and determine the existence of wet snow in the Austrian Alps by comparing the image that is mapped (σ_{map}) with a reference image (σ_{ref}) containing no snow or only dry snow. This relaxes the need to correct for incidence angle variations because relative values are used and repeat orbits are accurate. Wet snow is present in their study when σ_{map} divided by σ_{ref} is less than 0.9. Qualitative assessment indicates good accuracy. A similar approach is used by *Baghdadi et al.* [1997] for a study area in southeastern Québec, Canada. Wet snow is present when σ_{map} minus σ_{ref} is less than or equal to -3 dB and σ_{map} is between -18 and -11 dB. Applying this mapping algorithm to a totally snow free image, they find that less than 3% of no-snow pixels are incorrectly mapped as wet snow.

For a test site in northern Finland, *Koskinen et al.* [1997] are able to determine the relative fraction of snow-free ground within a pixel by comparing a SAR image to an image right before and after the melt season. Qualitative assessment gives good agreement with other observations.

Shi et al. [1994] find 80% agreement between wet snow cover derived from Landsat TM and C-band single-polarization SAR (airborne) in the Ötztal Alps in Austria. Using texture information, i.e., the standard deviation of the backscatter in a 9 × 9 pixel area, increases accuracy. The accuracy also increases using multipolarization SAR. This suggests improved mapping capability with the multipolarization ASAR sensor to be launched on Envisat in June 2001. *Shi et al.* [1997] use spaceborne imaging radar-C/X-band synthetic aperture radar (SIR-C/X-SAR), which was flown on the space shuttle in 1994. Using this multipolarization and multi-frequency SAR, they are able to distinguish dry snow from other surfaces at an alpine site in the Sierra Nevada. This shows a high potential once such sensors are available in space. A further promising approach is the use of interferometric techniques (see also section 3.2.2), using the phase of the SAR signal in addition to backscatter [*Shi et al.*, 1997; *Strozzi et al.*, 1999]. A coherence image shows the correlation of the phase between two SAR images and thus changes with time. Using coherence images, *Shi et al.* [1997] mapped dry and wet snow with an accuracy of better than 86% compared with a Landsat TM derived map.

2.3.2. Medium-scale mapping. The National Operational Hydrologic Remote Sensing Center (NOHRSC) publishes weekly snow charts with 1.1-km resolution for North America (Figure 4). These maps are available online at http://www.nohrsc.nws.gov/. Snow cover is mapped from AVHRR utilizing multiple channels (http://www.nohrsc.nws.gov/html/papers/theta/theta.htm). Each pixel represents a vector, the vector components being the digital numbers of the spectral bands. The angle between this vector and a reference vector is calculated and viewed as a value in an image. Similar areas cluster at a specific angle, which allows discrimination of snow-covered areas. AVHRR bands 3, 4, and 5 are used for snow-cloud separation, while AVHRR bands 1–4 are used to determine the extent of snow and clouds. Thus two thresholds have to be set manually by the analyst. There are no comprehensive studies examining the accuracy of the NOHRSC snow maps. This is a general problem for all snow-mapping algorithms. Accuracy determination would require reliable ground truth maps, which do not exist, especially for larger-scale and hemispheric snow maps.

In Norway the Norwegian Water Resources and Energy Directorate (NVE) produces snow maps from AVHRR using an algorithm developed by *Andersen* [1982]. AVHRR bands 3, 4, and 5 are used for snow/

cloud discrimination, while AVHRR band 2 is used for snow mapping. The value distribution is viewed in a histogram, and an upper limit for 100% snow cover is set from glacier or snow-covered areas, while the lower limit of 0% snow cover is set from water or land areas. Then the percentage of snow cover is interpolated linearly [*Schjødt-Osmo and Engeset*, 1997]. The Tromsø Satellite Station also provides snow maps of Norway based on *Andersen*'s [1982] algorithm. This is a simple and robust algorithm, which can be easily applied to the satellite images. As with the previous algorithm, however, accuracy determination is poor.

An algorithm, called SNOWMAP, has been developed for the MODIS sensor using the corresponding Landsat TM bands. On MODIS this algorithm will allow mapping of global snow cover automatically at a 500-m scale [*Hall et al.*, 1995a]. Maps can be created daily, cloud cover permitting. SNOWMAP is a straightforward algorithm with good results and is easier to implement than many of the other algorithms presented. Its big advantage will be the daily coverage while still providing maps at a 500-m scale. SNOWMAP is based on the normalized difference snow index (NDSI), which is calculated with at-satellite reflectance values rather than with raw, digital numbers:

$$\text{NDSI} = \frac{\text{MODIS band 4} - \text{MODIS band 6}}{\text{MODIS band 4} + \text{MODIS band 6}}. \quad (4)$$

The NDSI has been used previously by *Kyle et al.* [1978], *Bunting and d'Entremont* [1982], and *Dozier* [1989]. Since snow reflects more energy in the visible part than in the midinfrared, this ratio enhances the contrast between snow and bare ground. Additionally, the reflectance of clouds remains high in MODIS band 6 (1628–1652 nm). Thus the NDSI allows us to discriminate some clouds and snow. Snow is mapped for pixels with an NDSI greater than 0.4 [*Hall et al.*, 1995a; *Dozier*, 1989]. Since water bodies may have similar NSDI values, an additional requirement is introduced; the reflectance has to be larger than 11% in MODIS band 2 (841–876 nm) in order to be mapped as snow.

Comparing the SNOWMAP algorithm with an existing, validated snow map, *Hall et al.* [1995a] conclude that SNOWMAP is 98% accurate in identifying pixels that have more than 60% snow cover. Mixed pixels with less than 60% snow cover are mapped as bare ground. Errors are greater in forested areas, where vegetation masks the snow cover. *Klein et al.* [1998] therefore add an additional requirement, combining the NDSI with the normalized difference vegetation index (NDVI). If the NDVI identifies a pixel as a forested pixel, snow cover is assumed also for NDSI values lower than 0.4. In order to avoid mapping dark targets as snow with this method, the MODIS band 4 (545–565 nm) reflectance has to be larger than 10% in forested pixels. Applying this method results in a significant improvement in snow cover mapping relative to the original algorithm. A further error is

introduced due to the underestimation of snow cover in mountainous areas. Since the satellite looks at sloped surfaces with an angle, the pixel area is much smaller than the real area. *Hall et al.* [1995b] use a DEM with the SNOWMAP algorithm to adjust for this effect in Glacier National Park, Montana. The pixel area is corrected to real area using a correction factor, depending on topographic relief. Without this correction the snow cover would be underestimated considerably in high-relief areas [*Hall et al.*, 1995b]. This correction, however, is not presently implemented in the SNOWMAP algorithm.

2.3.3. Large-scale mapping. Between November 1966 and May 1999 the National Oceanic and Atmospheric Administration/National Environmental Satellite Data and Information Service (NOAA/NESDIS) provided weekly, large-scale snow cover maps of the Northern Hemisphere [*Robinson*, 1993], providing a valuable climatic record. The presence of snow was determined by visual analysis of the AVHRR images from the previous 7 days, using the most recent clear view of the surface. The observation is therefore biased toward the end of the week [*Basist et al.*, 1996]. If a particular region was cloud-covered for the entire week, the analyst used the previous week's snow cover [*Basist et al.*, 1996]. A cell was marked as snow-covered when 50% or more was snow-covered [*Robinson et al.*, 1993], while forests were assumed to be snow-covered if the surrounding areas were snow-covered [*Hall et al.*, 1995a]. The resolution was approximately 190 km [*Basist et al.*, 1996]. Between 1972 and 1991 the highest snow extent was in January, being on average 46.6×10^6 km^2, while the lowest extent was in August, with 3.9×10^6 km^2 [*Robinson*, 1993]. Some inconsistencies in area calculation due to different land masks before and after 1981 were identified by *Robinson* [1993].

Since February 1997, NESDIS produces a daily, Northern Hemispheric snow and ice chart instead on an improved 25-km scale (the NESDIS Interactive Multisensor Snow and Ice Mapping System (IMS)). Since June 1999, these snow maps (Figure 5) replace completely the previous AVHRR-based maps. The 15-month period, in which both maps were produced, was used to analyze differences between the two products, to provide a seamless transition between both products, and to ensure integrity of the long time series of data [*Ramsay*, 1998]. The new product, available at http://www.ssd.noaa.gov/, is based on imagery from various polar-orbiting and geostationary satellites as well as from snow maps from the Special Sensor Microwave Imager (SSM/I), which are discussed below, and surface information. A description of the IMS system is given by *Ramsay* [1998]. The absolute accuracy of the NESDIS snow maps for both algorithms presented above is uncertain, since the true snow extent is not known. However, using the same method over such a long time period (since 1966) reveals trends in snow extent. *Robinson et al.* [1993] report that monthly snow cover between 1972 and 1991 has been below normal since 1987

Figure 5. The National Environmental Satellite Data and Information Service (NESDIS) daily Northern Hemisphere snow and ice chart for Tuesday, November 7, 2000. These maps are produced using the Interactive Multisensor Snow and Ice Mapping System (IMS), which is operational since June 1999. Reprinted with permission from the Satellite Service Division (SSD) of NESDIS.

and that 1978 had the most snow (27.3×10^6 km^2) while 1990 had the least snow (27.3×10^6 km^2). The MODIS snow maps described above will be an advancement to the NOAA maps, since they will provide global snow maps on a much improved scale (500 m).

Passive microwave remote sensing allows snow mapping under cloudy skies because microwaves penetrate nonprecipitating clouds. The intensity of the radiation in the microwave part is, however, so low that the resolution of passive microwave sensors is of the order of tens of kilometers (15–25 km). Snow is identified by the attenuation of the known level of ground-emitted microwave radiation by the overlying snow cover due to volume scattering in the snowpack. Shallow or wet snow cover is difficult to identify. Shallow snow hardly attenuates the radiation, and regarding wet snow, only a small amount of liquid water (1%) causes surface scattering to dominate over volume scattering [*Bernier*, 1987; *Mätzler and Hüppi*, 1989]. This causes brightness temperatures to be higher, thus causing wet-snow pixels to be identified as snow-free [*Walker and Goodison*, 1993]. During times of snowmelt this can lead to apparent disappearance and reappearance of snow cover on successive satellite passes due to changing wetness conditions (Figure 6) [*Walker and Goodison*, 1993]. On ice sheets without bare ground, like Greenland, this brightness temper-

ature increase can be used for mapping areas of snowmelt [*Mote et al.*, 1993; *Abdalati and Steffen*, 1997].

NESDIS produces daily snow charts for the Northern Hemisphere from SSM/I, which are averaged into weekly snow products. A description of the algorithm is given by *Grody and Basist* [1996]. Snow cover is identified when the brightness temperature in the 19-GHz channel is higher than in the 37-GHz channel (or higher in the 22-GHz channel compared with the 85-GHz channel). The passive microwave algorithm has been adjusted to agree as best as possible with the AVHRR-derived hemispheric snow cover maps described above in order to preserve the continuity of this long time series [*Basist et al.*, 1996]. The daily SSM/I maps record transient snow cover that is not included in the weekly AVHRR maps and are not negatively influenced by persistent cloud cover. Snow in forested areas is underestimated by SSM/I. Snow cover in spring and summer is also underestimated in comparison with the AVHRR maps, because SSM/I has difficulties in observing melting snow. These differences between the AVHRR and SSM/I derived maps are discussed in more detail by *Basist et al.* [1996].

There also exist monthly snow cover charts of the Northern Hemisphere between 1978 and 1987 from the scanning multichannel microwave radiometer (SMMR) sensor [*Chang et al.*, 1990]. *Robinson* [1993] compares
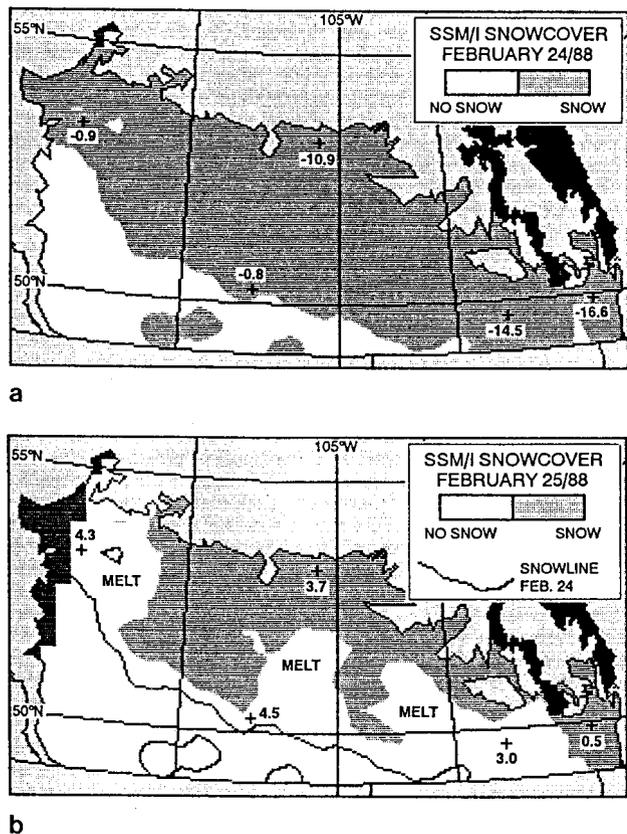
Figure 6. Canadian prairie snow cover derived from SSM/I for (a) February 24, 1988, and (b) February 25, 1988, showing snow (darker shading) and snow-free areas (white) [from *Walker and Goodison*, 1993]. Solid and lighter shaded areas are not mapped for snow. Air temperatures (°C) at synoptic stations at the time of the SSM/I orbit are plotted. The snow boundary extracted from Figure 5 (in Figure 6a) defines the area where the snow has "disappeared" due to possible wet snow conditions. Reprinted from the *Annals of Glaciology* with permission of the International Glaciological Society.

the differences between the SMMR and the AVHRR maps. Similarly to *Basist et al.* [1996] above, he finds that the SMMR maps underestimate snow cover, most likely because they do not recognize wet and shallow snow cover correctly. The differences are biggest in summer and fall, being just 20–40% of the visible AVHRR estimates in summer compared with 40–70% in fall and 80–90% in winter.

2.4. Snow Depth and Snow Water Equivalent (SWE)

Only the microwave region allows direct mapping of snow volume, because only in these wavelengths is there penetration through the snowpack. In the visible region, additional information is needed. *Cline et al.* [1998], for example, combine a snow depletion model with Landsat data to derive snow depth. The NOHRSC AVHRR snow maps, described earlier, are labeled by elevation, i.e., mapped by elevation zone. Thus approximate SWE maps are available using a simple linear relation of SWE versus elevation.

Multipolarization SAR, like the future ASAR or RADARSAT 2 sensors, may allow direct snow depth estimation. On the basis of model SAR simulation for snow conditions in the Sierra Nevada, *Shi et al.* [1990] find a relationship between snow depth and the ratio and also the difference of the vertically and horizontally polarized SAR signal. There have not been any further studies, however, examining this relation. A new method for estimating SWE of dry snow cover with interferometric techniques has just been presented by *Guneriussen et al.* [2000]. SAR sensors also record the phase of the wave signal. Even though the SAR backscatter is unaffected by dry snow, as discussed above, the radar wave will be refracted in the snow cover. Changes between two SAR images in time can therefore be seen as a change in phase, and *Guneriussen et al.* [2000] present a relation between this phase change and SWE, which they find supported by observations in the Heimdalen area of Norway. More studies testing this method against ground truth are needed. If successful, this method will provide a direct high-resolution SWE measurement from satellite, unaffected by cloud cover. One limitation of using SAR, however, is the low temporal resolution, generally covering one area not more than two times per month.

On a much larger scale, passive microwave remote sensing has been used to map snow depth or SWE. The low resolution (∼25 km) is good for daily, hemispherical snow mass observations. The microwave radiation stems from emission from the snow itself and from emission from the ground. This upwelling radiation is scattered by the snow grains in the snow such that the radiation is attenuated for a deeper snow cover. The deeper the snow cover is, the less radiation comes through, and lower brightness temperature is detected. Therefore an inverse relationship between snow depth and brightness temperature exists, implemented in algorithms by using the brightness temperature difference between the 18- and 37-GHz bands [*Chang et al.*, 1987; *Goodison and Walker*, 1995]. The agreement between satellite-derived snow depth and individual ground measurements is quite poor, as found by *Tait and Armstrong* [1996] comparing the algorithm by *Chang et al.* [1987] with ground data from the former Soviet Union. This, however, is also an effect of scale, assuming single measurements to be representative for a 25- × 25-km pixel. *Goodison and Walker* [1995], for their algorithm, find that areally averaged SWE values are within 10–20 mm of satellite-derived values. This is very good, given the poor agreement with point measurements.

Several effects cause the relation between brightness temperature and snow depth to break down, thus causing error. The scattering influence of the snow grains saturates at snow depths greater than 50–100 cm. Brightness temperature therefore no longer changes with depth for deep snow cover, leading to an underestimation of snow depth in some areas in winter and early spring [*Tait and Armstrong*, 1996]. Shallow snow cover

hardly attenuates the microwave, and wet snow, as mentioned above, is not distinguished from bare ground and does not give volume scattering necessary for snow volume determination. A wet-snow indicator based on the polarization difference in the 37-GHz band distinguishes wet snow from ground [*Walker and Goodison*, 1993]. This allows more accurate estimation of snow extent, but not estimation of SWE for wet-snow areas.

Additionally, the brightness temperature depends not only on snow depth, but to a large extent also on grain size, since for the same snow depth larger snow grains increase volume scattering and thus decrease brightness temperature. This is seen in the results from *Hall et al.* [1986] and *Chang et al.* [1987], where larger depth hoar crystals in Alaska give a lower brightness temperature, leading to an overestimation of snow depth. Since algorithms have successfully related snow depth to brightness temperature without considering grain size, it has been assumed that for a given region there is a relation between snow depth and grain size [*Armstrong et al.*, 1993]. Another source of error stems from green forest cover above the snow-covered ground, which emits radiation itself, leading to increased brightness temperatures and an underestimation of snow depth. As a consequence, *Tait* [1998] developed a relation for different landscape types, considering areas of large grain size, areas of snowmelt, vegetated areas, and mountainous areas. *Foster et al.* [1997] adjusted the algorithm of *Chang et al.* [1987] for different continental areas, which considerably increased the agreement with snow-depth maps created by the U.S. Air Force from ground data. In this study the algorithm by *Chang et al.* [1987] underestimated snow mass by up to 60% compared with ground measurements. For the same year and the same area, the algorithm by *Foster et al.* [1997] underestimated snow mass generally by less than 30%.

3. REMOTE SENSING OF GLACIERS AND ICE SHEETS

Glaciers have for a long time been recognized as sensitive indicators of climate change. Their importance to climate research is especially significant, because they contain a considerable part of the world's fresh water and therefore contribute to sea level change. The most obvious indicator is the advance or retreat of front position, which is caused by changes in glacier mass balance. The response time to such changes, however, is highly variable, depending on both direct climate forcing and individual physical conditions such as glacier size, topography, and ice temperature [*Paterson*, 1994]. The equilibrium line position is more directly affected by annual perturbations and is therefore a very important part of glacier studies.

In addition to direct observations of glacier front positions, other aspects of glaciers also provide insight to our understanding of the driving mechanisms behind their behavior. For example, information about ice ve-

locity, temperature, and glacier facies is a valuable addition to our understanding of glaciers and ice sheets. Complementary information on remote sensing of ice sheets is given by *Bindschadler* [1998]. The following sections will provide an update on this topic, which is especially evident in the section on glacier facies and equilibrium line detection, as well as in our additional coverage of studies on small glaciers. In comparison, our emphasis is more on the principles behind each method (e.g., SAR interferometry).

3.1. Glacier Facies and Equilibrium Line

In its simplest form, a glacier can be divided into an area that gains mass, the accumulation area, and an area that loses mass, the ablation area. Accumulation and ablation areas are separated by the equilibrium line, where the net balance is zero. Changes in the equilibrium line's position give important information on the glacier's status. Accumulation and ablation areas can be further divided into glacier facies, these being distinct zones with distinct characteristics in the surface layers of a glacier. A short description of glacier facies can be seen in Figure 7 and later in this section. Detailed information on glacier facies is given by *Paterson* [1994] and *Benson* [1996].

Satellite imagery can identify several distinct zones on a glacier. However, these zones develop and change location in time and are therefore not always identical with glacier facies. The term radar zone has been suggested for these variable zones on SAR imagery [*Smith et al.*, 1997; *Forster et al.*, 1996], but the situation is the same for visible imagery. In most studies, insufficient ground data make interpretation of the observed zones difficult, and the question remains on how much these zones match the actual glacier facies.

Visible imagery taken at the end of the ablation season may allow determination of accumulation and ablation areas [e.g., *Hall et al.*, 1987; *Rott and Markl*, 1989; *Williams et al.*, 1991; *Parrot et al.*, 1993]. *Williams et al.* [1991] identify three distinguishable zones on Landsat images of Icelandic glaciers, which they name snow facies, ice facies, and slush zone. The slush zone is more a transition zone of wet snow, while snow and ice facies appear as distinct peaks in the distribution of reflectance values. *Hall et al.* [1987] find the same three zones on glaciers in the Grossglockner glacier group and believe that the slush zone represents some or all of the wet-snow facies. *Parrot et al.* [1993] study a glacier on Svalbard with SPOT images. They correct albedo for topographic effects and adjust for pixels in shadowed areas with the help of a DEM. Thus they find the snow line, which they assume to be within 40 m of altitude to the equilibrium line due to the superimposed ice facies separating these two lines. Studying the same glacier, *Winther* [1993b] also finds that these two areas have distinct reflectance values.

Fresh snowfall may obscure the facies and produce erroneous results [*Hall et al.*, 1987]. *Williams et al.* [1991]
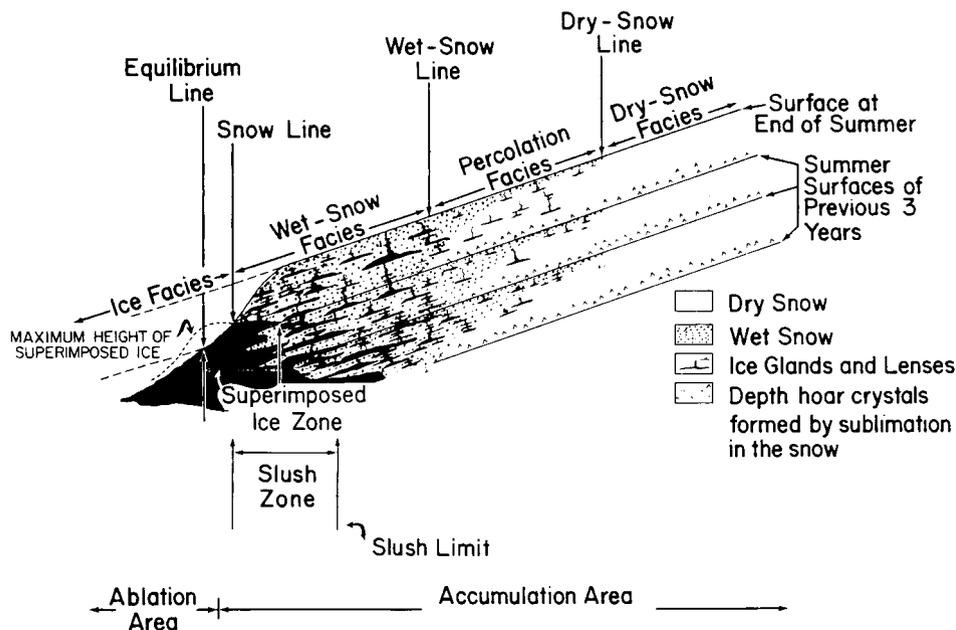
Figure 7. Generalized cross section of glacier facies [from *Benson*, 1996]. Negligible melt occurs in the dry-snow facies. Some melting occurs in the percolation facies, forming ice lenses when it refreezes. The entire year's accumulation is raised to the melting point and wetted in the wet-snow facies, and some meltwater may percolate into previous year's layers. Extensive melting occurs in the superimposed-ice facies, and a continuous mass of ice is formed. The bare-ice facies represents the ablation area. Reprinted with permission from the Cold Regions Research and Engineering Laboratory (CRREL).

cite an example where early snowfall down to lower elevations masked the real late-summer snow line. Debris may improve snow line detection by enhancing the contrast between accumulation and ablation areas, but it also can make it impossible to distinguish glacier ice from moraine. Both *Williams et al.* [1991] and *Hall et al.* [1987] find TM band 4 (800–1110 nm) the most useful for analysis because it is sensitive to grain size. They use the TM4/TM5 ratio for their studies, which also improves the contrast between glacier and terrain.

Visible imagery cannot separate percolation facies from the wet-snow facies [*Williams et al.*, 1991]. This transition is defined by water percolating into the previous year's layers, as such having no surface manifestation. The dry-snow facies may be discernible from the wet-snow facies, but it actually depends also on observations below the snow surface, i.e., the presence or absence of slightly wet snow in deeper layers.

Most studies for detection of equilibrium line and glacier facies have been done with SAR rather than with visible imagery. Glacier studies using SAR are best done with winter images, when no melting snow overlies the characteristic backscatter of a particular zone. The dry winter snow cover is invisible to the SAR, and the end-of-summer situation is normally preserved. This gives a much larger time window for image acquisition, while the narrow end-of-summer window for acquisition of visible imagery is easily affected by changing surface conditions (e.g., fresh snow) or cloud cover.

Studies on smaller glaciers usually find a distinct

boundary on the SAR images, which often was interpreted to be the equilibrium line [e.g., *Hall et al.*, 1995c; *Engeset and Weydahl*, 1998]. However, most of these studies lack ground observations, and there has been doubt recently that these studies indeed have identified the equilibrium line. Some believe they have instead identified the firn line. The firn line is created by old snow layers from several previous years of snow accumulation and is the dividing line between these old layers and the bare ice zone. The present year's accumulated snow lies on top of this old stratigraphy, and the equilibrium line may therefore be obscured by the old firn, since snow and firn look similar on SAR images. This is seen by *Hall et al.* [2000] for Hofsjökull, Iceland.

A good example of this situation can be found on Kongsvegen glacier on Svalbard. *Engeset and Weydahl* [1998] studied Kongsvegen using an ERS SAR image and found excellent agreement between equilibrium-line altitude and an observed boundary on the SAR image (Figure 8). *Engeset* [2000], however, studied an 8-year time series of SAR images from the same glacier and found that this apparent agreement has been accidental. The observed boundary occupied the same position year after year, and *Engeset* [2000] conclude that this line represents the average firn-line altitude. Similarly, M. König et al. (Equilibrium and firn-line detection on Austre Okstindbreen, Norway, with airborne multipolarization SAR, submitted to *Journal of Glaciology*, 2000; hereinafter referred to as submitted manuscript, 2000) present field observations and photographic evidence for
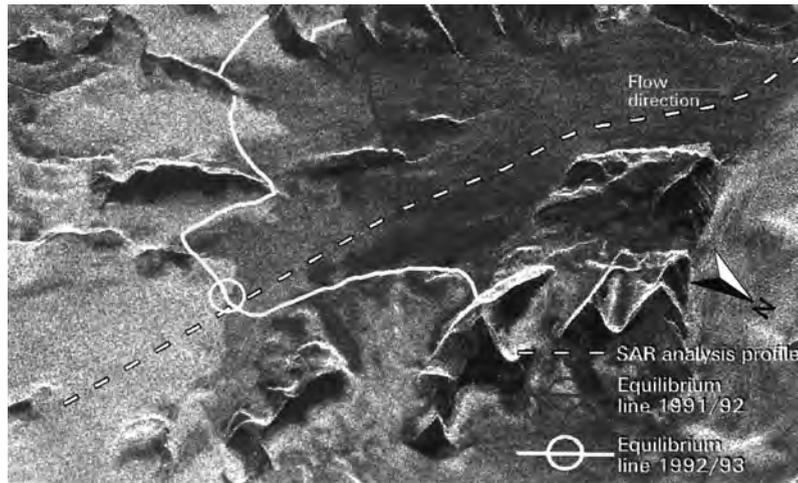
Figure 8. ERS-1 synthetic aperture radar (SAR) image from January 19, 1994, covering Kongsvegen glacier [from *Engeset and Weydahl*, 1998]. The boundary between the lighter and darker shaded areas to the left is the boundary, which first was assumed to be the equilibrium line, but is in fact the firn line (see text). The equilibrium lines estimated from stake measurements from 1991–1992 and 1992–1993 are superimposed and extrapolated along isoelevation. The circles mark intersections with mass balance measurement profiles. SAR image data were provided by the European Space Agency. Reprinted with permission from the Institute of Electrical and Electronics Engineers (© 1998 IEEE).

Austre Okstindbreen, Norway, showing that SAR images show the firn line rather than the equilibrium line. Monitoring the firn line, which appears to be easily detectable on SAR images due to strong difference in backscatter between ice and firn, will still be a valuable source of information. The firn line itself is not affected by yearly variations in equilibrium-line altitude; a permanent change, however, in the average equilibrium-line altitude will eventually result in a change in firn-line altitude. The firn line therefore seems to smooth out short-term variations and to show trends of larger timescales. Eventually, this may call for the development of correlation factors between firn-line altitude (FLA) and mass balance in contrast to today's use of equilibrium-line altitude (ELA) in order to use SAR for routine mass balance monitoring (M. König et al., submitted manuscript, 2000). The connection between firn-line altitude and mass balance, however, needs further investigation.

On large ice sheets it appears to be possible to detect not only the firn line, but also different glacier facies. A concise overview of glacier facies as seen with SAR imagery is given by *Fahnestock et al.* [1993]. *Partington* [1998] uses multitemporal images, acquired at different seasons, to define a signature for each facies for Greenland and Alaskan glaciers. A study with airborne, multifrequency multipolarization SAR on Greenland has been done by *Jezek et al.* [1993]. Temporal evolution of backscatter zones during summer was examined by *Rees et al.* [1995] for the Austfonna ice cap in Svalbard and by *Smith et al.* [1997] for the Stikine ice field in British Columbia. Observations made with C-band SAR were interpreted as follows for the different facies:

3.1.1. Dry-snow facies. A dry-snow facies is found only in Greenland and Antarctica and on some glaciers in Alaska and Svalbard at high elevations. The absence of any surface melt and the consequently small snow grain size cause little volume scattering and thus a low backscatter value [*Fahnestock et al.*, 1993]. This is found in all seasons [*Partington*, 1998]. Backscatter variations and some areas of higher backscatter within the dry-snow facies may be related to grain size variations, specifically large depth-hoar crystals forming due to strong temperature gradients in areas of lower accumulation [*Partington*, 1998].

3.1.2. Percolation facies. Ice lenses in the snow cover due to occasional melt cause a very high backscatter [*Bindschadler and Vornberger*, 1992; *Fahnestock et al.*, 1993] during the winter months. However, during the melt season, the surface of the percolation facies becomes wet and the backscatter drops to very low values.

3.1.3. Wet-snow facies. *Fahnestock et al.* [1993] observe a narrow zone of intermediate brightness due to snowmelt in Greenland. *Bindschadler and Vornberger* [1992], also studying Greenland, see a distinct boundary at the percolation facies, the wet-snow facies being a bright area with dark patches (slush around surface lakes). *Partington* [1998] sees three zones within the percolation and wet-snow facies. At high elevations a high backscatter is found in all seasons because hardly any melt is present. In middle elevations the backscatter is high in winter and spring but low in late summer due to surface melt. In low elevations, backscatter is high in winter but low in spring and summer due to surface melt.

3.1.4. Superimposed-ice facies. On temperate glaciers the late-summer snow line is nearly coincident with the equilibrium line. On some glaciers, however, a zone of superimposed ice separates the equilibrium line from the snow line. This superimposed-ice facies has not

yet been identified with SAR images. *Bindschadler and Vornberger* [1992] consider it virtually impossible to detect this facies since both bare-ice facies and superimposed-ice facies consist of bare ice. *Marshall et al.* [1995], however, report to have detected the superimposed-ice facies on Ayerbreen, Svalbard, due to marked differences in surface roughness of bare and superimposed ice.

3.1.5. Bare-ice facies. According to *Bindschadler and Vornberger* [1992] and *Fahnestock et al.* [1993], the smooth ice surface, being a specular reflector, causes a lower backscatter than the wet-snow facies in winter. In summer, however, the backscatter of the bare-ice facies appears higher due to the presence of melt and low backscatter in the wet-snow facies. *Partington* [1998] similarly finds a higher backscatter in September than in June and December from the bare-ice facies. In contrast to the above, he sees ice as a strong scatterer, for which the high backscatter is attenuated in winter by overlying snow. Both statements seem to be valid. Backscatter differences in the wet-snow facies between wet summer and dry winter conditions are strong. Also, the bare-ice surface can have a rough or smooth surface structure in different years, resulting in different backscatter. For example, rain on the surface followed by cold weather results in a smoother ice surface, while rain on the surface followed by snowfall results in a rougher surface (J.-O. Hagen, personal communication, 2000). Furthermore, refrozen meltwater originating from the winter's first snowfall can fill surface irregularities and make a rough glacier-ice surface appear smooth in winter. Crevasses in the bare-ice facies undoubtedly appear as bright areas [*Fahnestock et al.*, 1993; *Engeset and Weydahl*, 1998]. The boundary between the bare-ice facies and the wet-snow facies is distinct, which allows the determination of the snow line [*Bindschadler and Vornberger*, 1992; *Fahnestock et al.*, 1993; *Hall et al.*, 1995c; *Engeset and Weydahl*, 1998].

3.1.6. Nonglacierized areas. It is often difficult to discriminate glacier ice from the surrounding moraine using SAR data due to similar backscatter characteristics [e.g., *Shi and Dozier*, 1993]. *Engeset and Weydahl* [1998] could discriminate nonglaciated ground on all images, but did best in spring. Ice-margin lakes, if present, provide a way to detect the edge of a glacier using SAR and even Landsat data [*Hall et al.*, 1995c].

3.2. Glacier Velocity

3.2.1. Glacier velocity with feature tracking. Glacier velocity can be determined with sequential satellite imagery by observing the movement of surface features, such as crevasses, in time. This can be done simply by visual observation [*Lefauconnier et al.*, 1994]. *Lucchitta et al.* [1993] coregister sequential images, one in the red channel, one in the green channel. Features that have moved will appear as tones of green or red. Moving of one image over the other until a moved

feature matches again results in a yellow tone for this feature, and the moved distance can be determined.

Scambos et al. [1992] developed an automated method, which was successfully applied in many studies in Antarctica [*Scambos and Bindschadler*, 1993; *Bindschadler et al.*, 1994, 1996; *Lucchitta et al.*, 1995; *Rosanova et al.*, 1998] (see Figure 9). A comparable method was used by *Rolstad et al.* [1997] for a surging glacier in Svalbard. Sequential images are taken at the same time in order to have similar illumination. Additionally, a principal component image is used. A principal component analysis done on the image bands results in new image bands, where the first band (PC1) now contains most image variation and thus enhances topography. The images then are split in a long wavelength and a short wavelength image using high- and low-pass filters. The long wavelength image contains topographic effects only, which have a low spatial frequency, and is used to coregister images. This approach is necessary on ice sheets, where no nonglaciated terrain is available to coregister images. The short wavelength image is used to track small, sharp features. A chip (16 × 16 or 32 × 32 pixels, i.e., a sidelength of 960 or 2560 m for Landsat TM) from the first image, containing a feature, is moved over the second image. The correlation is calculated and a match is found where correlation is highest. Since a whole chip is matched and not a single pixel, the matching will be accurate to better than pixel size. *Scambos and Bindschadler* [1993] give an accuracy of ∼6 m yr^1, which improves significantly in areas with many measurements. *Lucchitta et al.* [1993] find an error of as little as 20 m yr^{-1} when images separated by more than 10 years are used. *Frezzotti et al.* [1998] compare velocities derived by feature tracking with GPS inferred velocity measurements. They find good agreement, with maximum differences of 15–20 m yr^{-1} (Figure 10). Such errors, of course, are more significant on small glaciers with lower velocities (∼100–150 m yr^{-1}, sometimes much less), but of little significance for large outlet glaciers with velocities of 400–1000 m yr^{-1} [*Frezzotti et al.*, 1998].

All the studies have used Landsat imagery, except that of *Lucchitta et al.* [1995], who successfully used this method on SAR imagery. Comparing the Scambos method with visual tracking of features with repeat photogrammetry, *Whillans and Tseng* [1995] conclude that the "machine beats the human." The large number of tracked features that an automated method is able to process results in a much more detailed velocity field.

Bindschadler et al. [1996] also calculate discharge flux of Ice Streams D and E in Antarctica by combining the velocity measurements with transverse depth profiles collected by airborne radar. Strain rates can also be calculated from the obtained velocities [e.g., *Bindschadler et al.*, 1996].

3.2.2. Glacier velocity using SAR interferometry. The possibility of using SAR interferometry to determine glacier velocity was discovered by R. M. Goldstein
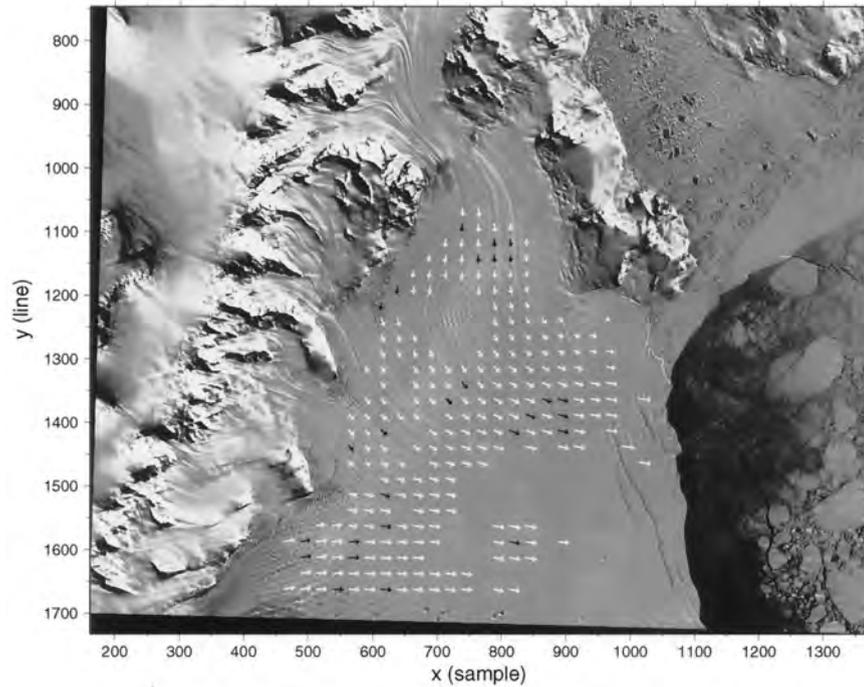
Figure 9. Landsat thematic mapper (TM) image collected on November 5, 1989. The plotted velocity field is derived from a multispectral scanner–TM image pair using cross correlation to track features by *Scambos et al.* [1992]. Vector lengths correspond to actual displacements over the 3.68-year interval. Vector grid spacing is 25 pixels (1425 m). Solid vectors are those in common with another data set (Kosmos-MSS image pair). The coordinate system refers to image pixels (60 m per pixel). [From *Bindschadler et al.*, 1994]. Reprinted from the *Annals of Glaciology* with permission of the International Glaciological Society.

after the launch of ERS-1 [*Goldstein et al.*, 1993]. A detailed description of the theory of SAR interferometry is given by *Fatland and Lingle* [1998].

Radar basically measures two kinds of information. The amplitude of the signal is influenced by the target properties, and the time delay of the signal gives the distance between radar and target. The distance between sensor and target is called the range. A SAR sensor does not record time delay but records the phase of the reflected wave. The phase information of a single SAR image is random and of no use. However, two SAR images taken from an orbit separated by a small distance will each have a different distance from sensor to a same target. Subtracting the phases of both images results in an interferogram, whose phase contains the difference in range. The interferogram has its phase value displayed in every pixel; thus phase variations (i.e., fringes) from pixel to pixel are visible (Plate 1).

Assuming no movement of a target, the phase in an interferogram is influenced by geometric effects and the topography. Having removed geometric effects, it is possible to calculate the elevation of a target and create a digital elevation model (DEM). For this the range and the baseline (i.e., the distance between the two satellite orbits) need to be known. Because satellite orbits are not known well enough to determine the baseline, the baseline is determined iteratively. This results in an effective baseline, which compensates for errors and thus works

better than the true baseline [*Joughin et al.*, 1996a]. Inaccuracy due to baseline errors is discussed by *Joughin et al.* [1996a].

Subtracting the phases of the two images results in a 2π ambiguity, because the phase values do not continue beyond 2π but start again with zero (Figure 11). In other words, a phase difference of $5\pi/2$ looks the same as $\pi/2$, because $5\pi/2 - 2\pi = \pi/2$. Resolving this 2π ambiguity is called "unwrapping the phase," for example, by adding or subtracting 2π to eliminate discontinuities (Figure 11). Determination of high velocities needs short temporal baselines (e.g., 1 day between images for 100–1500 m yr^{-1}); otherwise phase differences are so large that the phase cannot be unwrapped any longer. Determining low velocities benefits from having longer temporal baselines [*Joughin et al.*, 1998].

All the above is valid when no target is moving. For a moving target, the phase is additionally influenced by the translation of the target. The phase due to topography has to be extracted to get the velocity. If a precise DEM and accurate orbit data are available from the study area, then a synthetic (artificial) interferogram containing only the topographic phase can be made [*Joughin et al.*, 1996a, 1998; *Mattar et al.*, 1998]. The synthetic interferogram is then subtracted from the real interferogram, resulting in an interferogram that contains only the phase term due to translation.
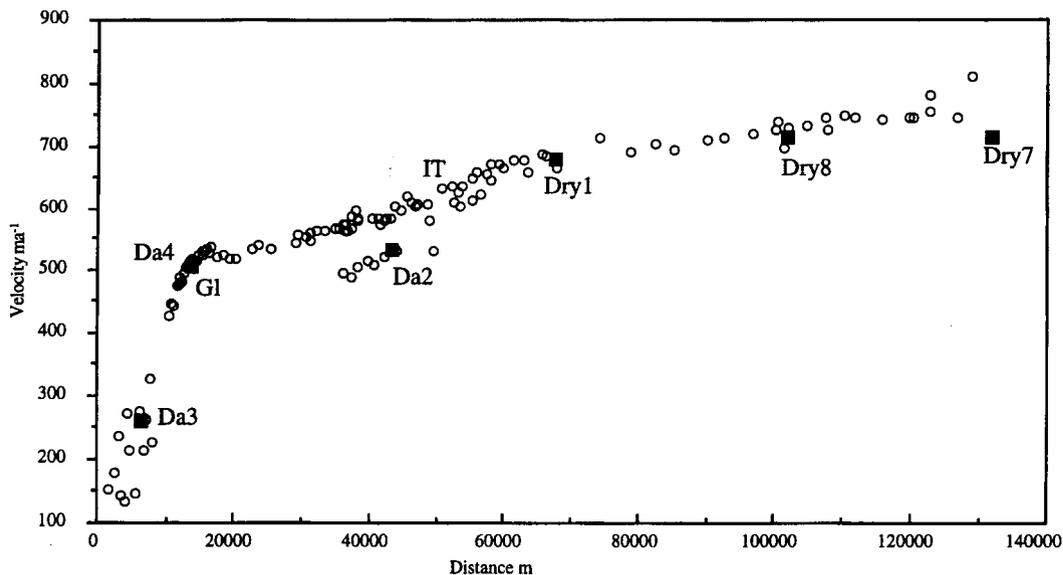
Figure 10. Ice velocity along a corridor (1.5 to 12 km wide) on David Glacier-Drygaslki Ice Tongue, Antarctica, following the southern stream [from *Frezzotti et al.*, 1998]. Solid squares, labeled with the site names, are surface GPS-survey velocities, while open circles are velocities derived with feature tracking from sequential Landsat TM images. Reprinted from the *Annals of Glaciology* with permission of the International Glaciological Society.

If surface topography is unknown, two interferograms are needed to extract the translation phase term. This approach was used, for example, by *Joughin et al.* [1998] and *Fatland and Lingle* [1998]: Images 1 and 2 result in interferogram A. Images 3 and 4 result in interferogram B of the same site some time later. Assuming that the target, i.e., the glacier, moves with constant velocity, then it moved Δx between the acquisition of images 1 and 2 and moved the same distance Δx between the acquisition of images 3 and 4. Subtracting interferogram B from interferogram A cancels the phase term due to translation, leaving only the topographic phase in the differential interferogram C. Subtracting C from A again gives an interferogram containing only the translation phase term.

The velocity determined from the translation, however, is only translation along line of site from sensor to target, i.e., the projection of the three-dimensional (3-D) velocity along this line. Having an interferogram from one look direction only requires two further assumptions. Having two interferograms from two look directions, i.e., an ascending and a descending pass, requires only one additional piece of information. Having three look directions is theoretically only possible with airborne SAR. Most studies assume ice flow parallel to the glacier surface [*Joughin et al.*, 1996a, 1998; *Rignot et al.*, 1996; *Fatland and Lingle*, 1998; *Mattar et al.*, 1998] as a first assumption and flow either along the steepest slope [*Joughin et al.*, 1996a; *Mattar et al.*, 1998] or parallel to the valley walls [*Fatland and Lingle*, 1998] as a second assumption. *Mattar et al.* [1998] find good agreement with in situ measurements. Having two look directions,

Mattar et al. [1998] examined the three possible cases for the one needed assumption. The first assumption, flow along the steepest slope, failed in a glacier bend; the second assumption, flow along the centerline, failed in some places of complex flow; and the third assumption, flow parallel to surface, failed in areas of high vertical velocity (accumulation/ablation area). Generally, however, they find good agreement with in situ measurements.

Rignot et al. [1996] found that interferometry-derived velocities and velocities by feature tracking complement each other and overlap. Velocity accuracy from interferometry is generally better than with feature tracking and usually of the order of a few meters in the studies above. *Joughin et al.* [1996a] compare with nonmoving ground (zero velocity) and find an error of -0.07 m yr^{-1} with a standard deviation of 2.1 m yr^{-1}. We refer to *Mattar et al.* [1998] for further discussion on accuracy and comparison with in situ measurements. For interferometric techniques a period of a few days between the images is sufficient, compared with years for feature tracking. Additionally, interferometry gives velocity values at any point on the glacier, while feature tracking depends on visible surface features and may not be possible in homogeneous areas without distinct surface structures (such as undulations or crevasses).

3.3. Glacier and Ice Sheet Topography

3.3.1. Glacier/ice sheet topography with satellite altimetry. Radar altimetry does not provide satellite images but is a direct measurement of elevation. Figure
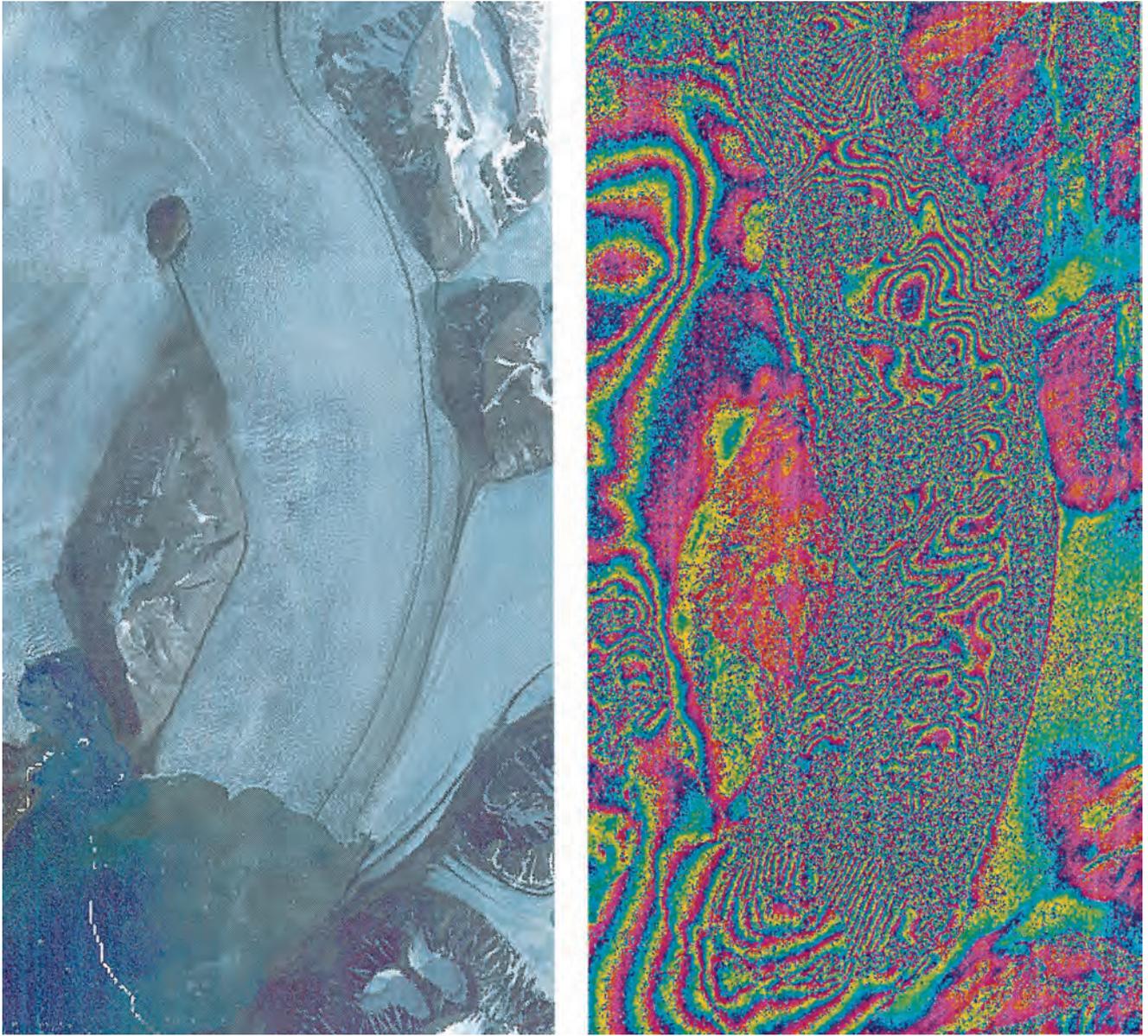
Plate 1. On the left is a SPOT satellite image of the fast flowing Kronebreen, Svalbard, from August 1996, and on the right is an interferogram of the same area from February 1995. Parallel colored bands (fringes) show movement of the glacier, moving perpendicular to these fringes. No fringes are seen for the terrain, since this effect has been removed. Fringes on the ocean are due to the moving sea ice. Note also that the much slower flowing Kongsbreen, to the left of Kronebreen, and Kongsvegen, to the right, have fewer fringes. The images are ~10 km across, and the lower left corner is at ~79°N, 12°20′E (unpublished material from K. Eldhuset et al., ERS tandem INSAR processing for DEM generation, glacier motion estimation and coherence analysis on Svalbard, submitted to *International Journal of Remote Sensing*, 2000).

12 shows this method for a flat surface. A radar pulse is emitted toward the ground, and the distance between satellite and ground (i.e., the range) is determined from the time delay of the return signal. The emitted pulse strikes the surface, illuminating a circular area (the pulse-limited footprint), which increases in time and causes the leading edge in the return signal. Afterward, within the beam-limited footprint, the return energy decreases. The elevation, calculated from range and the known orbit position, is the average elevation within the

pulse-limited footprint, typically having a size of ~2 km. An example is shown in Figure 13.

Retracking algorithms are used to detect the leading edge in the return signal. *Davis* [1996] compares two such commonly used algorithms. A correction needs also to be applied for sloped surfaces. Unlike in Figure 12, the first return from sloped surfaces does not come from the nadir point right below the satellite, but from the highest and thus the closest point to the satellite. The effectively measured footprint is thus displaced by up to

Glacier center line phase profile
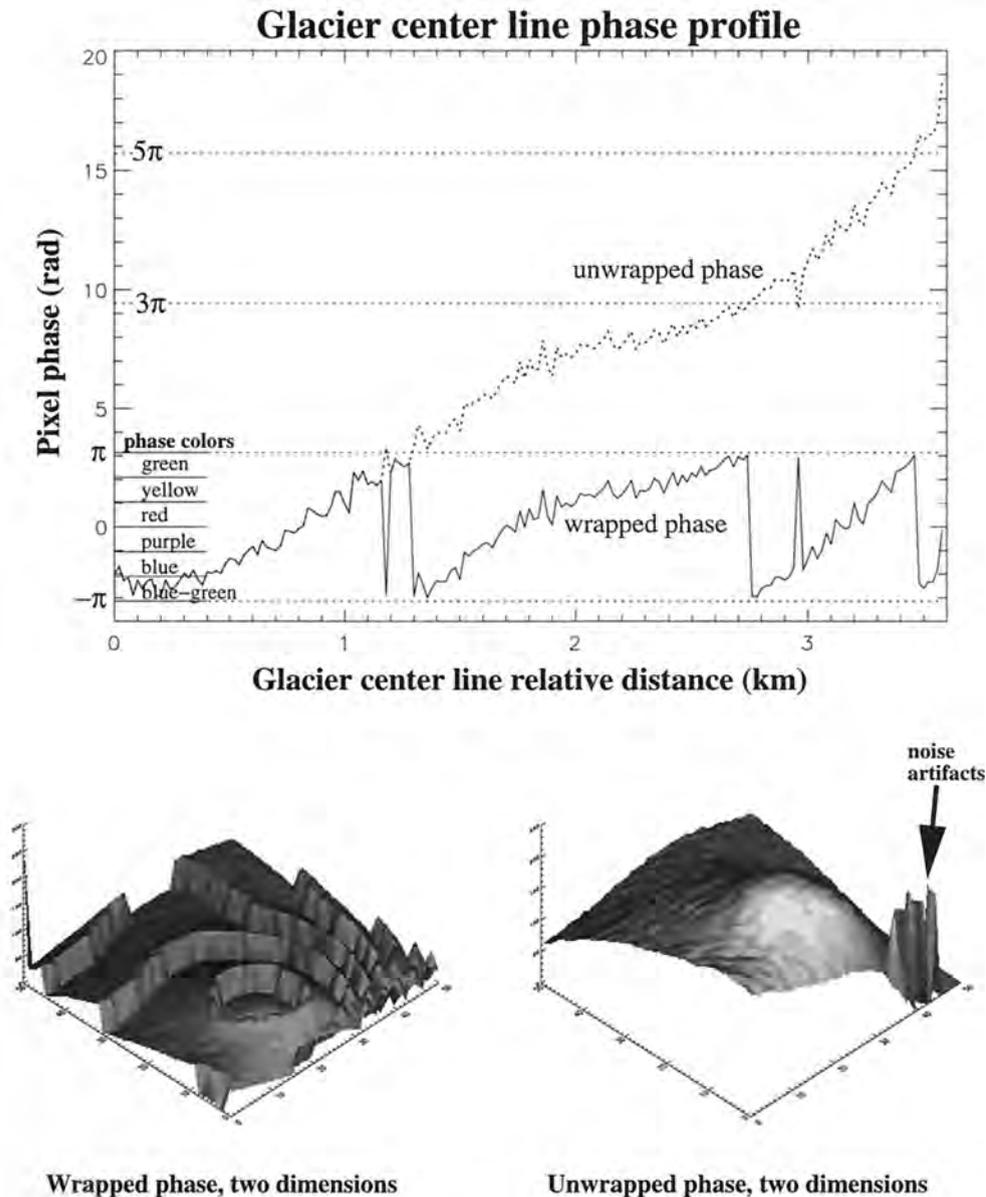
Figure 11. Phase unwrapping in one and two dimensions [from *Fatland and Lingle*, 1998]. Subtracting the phases of two images results in a 2π ambiguity, because the phase values do not continue beyond 2π but start again with zero. Resolving this ambiguity is called "unwrapping the phase." Jagged nature of the centerline plot is indicative of data noise rather than of variations in velocity. Reprinted from the *Journal of Glaciology* with permission of the International Glaciological Society.

several kilometers, lying anywhere within the beam-limited footprint. We refer to *Bamber* [1994a] for a discussion on retracking and slope correction.

Altimetry-derived elevation has been compared with ice shelf elevation inverted from Antarctic ice thickness data [*Bamber and Bentley*, 1994], airborne altimetry data in Greenland [*Ekholm et al.*, 1995], GPS-derived elevation in Antarctica [*Phillips et al.*, 1998], and airborne laser altimetry in Greenland [*Bamber et al.*, 1998]. Agreement is usually within a few meters (<3 m) for flat surfaces but increases for larger slopes to mean differences of around 10 m for 0.7° slopes [*Ekholm et al.*, 1995;

Bamber et al., 1998]. In general, errors can be caused by inhomogeneous terrain, uncertainties in satellite-orbit position, and penetration of the radar pulse into the surface layer. The latter can be up to 3.3 m [*Ridley and Partington*, 1988].

Altimetry has been used for creating elevation maps of Antarctica [*McIntyre*, 1991; *Bamber*, 1994b; *Legrésy and Rémy*, 1997; *Herzfeld and Matassa*, 1999] and Greenland [*Bindschadler et al.*, 1989], and also for detecting elevation changes over time in these areas [*Zwally et al.*, 1989; *Herzfeld et al.*, 1997; *Lingle and Covey*, 1998]. The spatial resolution of such elevation maps is of the order
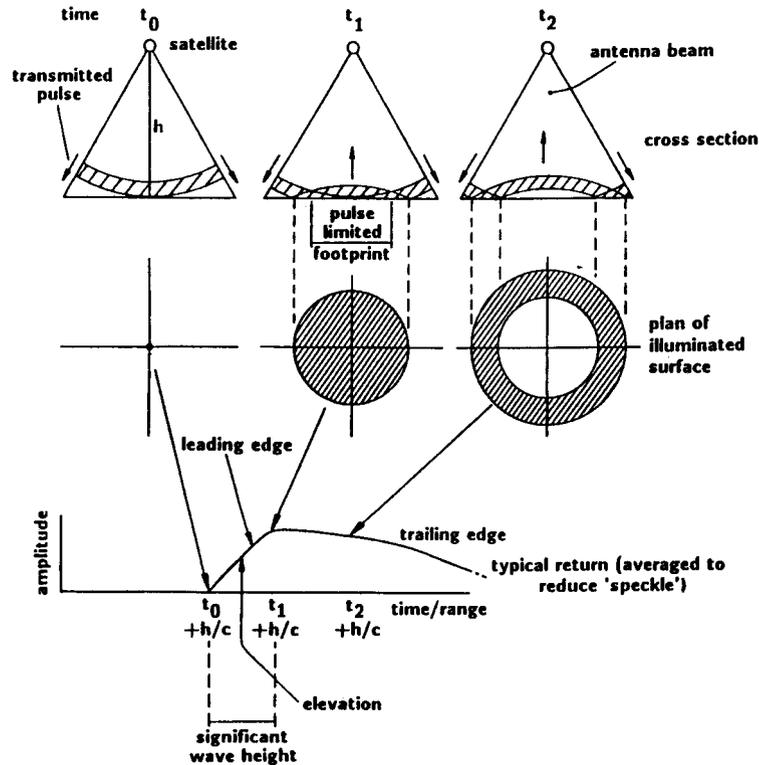
Figure 12. The interaction of an altimeter radar pulse with a horizontal and planar surface, from its initial intersection (t_0), through the intersection of the back of the pulse shell with the surface (t_1), to the stage where the pulse begins to be attenuated by the antenna beam (t_2). The return is from the surface only. [From *Ridley and Partington*, 1988]. Reprinted from the *International Journal of Remote Sensing* (www.tandf.co.uk/journals) with permission from Taylor and Francis.

of 10–20 km. Snowpack characteristics can also be mapped due to different penetration of the radar signal, affecting the returning waveform [*Partington et al.*, 1989; *Legrésy and Rémy*, 1998].

3.3.2. Glacier/ice sheet topography with SAR interferometry. SAR interferometry, as discussed earlier, can be used to generate DEMs. Interferometric DEMs show more detail than topography from radar altimetry due to higher spatial resolution, for example, 80 m versus 10 km as seen in Figure 14 [*Joughin et al.*, 1996b]. Interferometric DEMs, however, need known tie points for accurate elevation. *Joughin et al.* [1996b] determine topography in Greenland with an absolute elevation accuracy of about 4 m, having a spatial resolution of ~80 m. *Unwin and Wingham* [1997] report an accuracy of 8- and 40-m spatial resolution for their DEM of Austfonna ice cap, Svalbard. Interferometry has also been used to study the migration of the hinge line and tidal motion of floating ice stream tongues in Greenland and Antarctica by *Rignot* [1996, 1998].

3.4. Mapping Glaciers, Glacier Change, and Characteristics

Remote sensing allows mapping of glacier extent and surface features on large scales not nearly possible with ground observations. Many studies have been conducted by pure visual interpretation of satellite images, i.e., with little or no image processing. *Dowdeswell and Williams* [1997] identify surge-type glaciers from surface features such as looped moraines and crevasses. *Dowdeswell et al.* [1995] identify ice divides and drainage basins from visible as well as SAR imagery. *Hambrey and Dowdeswell* [1994] derive the flow directions of an Antarctic ice shelf from surface features (foliation, crevasses, moraines).

The visible bands are more suitable than infrared bands for studying topographic features. This observation is supported by doing a principal component analysis with the image bands as input variables. The first principal component image PC1 contains most of the image variance due to topography and is dominated by the visible bands [*Orheim and Lucchitta*, 1988; *Winther*, 1993a]. A PC1 image thus enhances topographic effects and is therefore often superior to the visible bands themselves. The PC2 image is mostly related to the Landsat shortwave infrared bands (TM bands 5 and 7) and enhances surface characteristics not seen in the visible, like patterns due to surface grain-size variations [*Orheim and Lucchitta*, 1987; *Winther*, 1993a]. Band ratioing (4/5; 2/5; 4/2) reveals features like dry water courses and frozen lakes [*Winther*, 1993a].

Efforts are under way to create coastal-change and glaciological maps of the entire perimeter of Antarctica
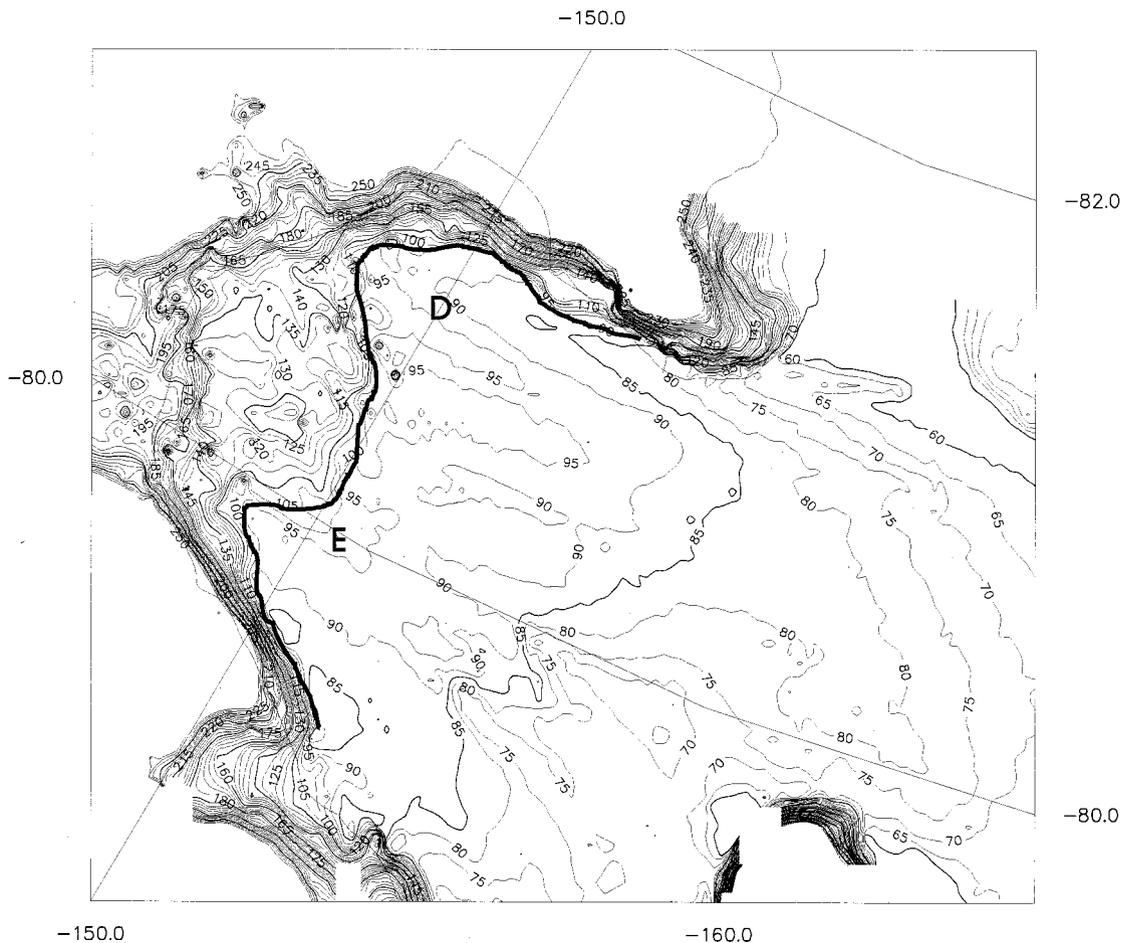
Figure 13. Map of surface elevations (in meters above sea level) on the ice plain of Ice Streams D and E, and the neighboring part of the ice shelf [from *Bamber and Bentley*, 1994]. Elevations above 250 m are not plotted. The approximate location of the grounding line, from the break in the slope, is shown as a bold solid line. Reprinted from the *Annals of Glaciology* with permission of the International Glaciological Society.
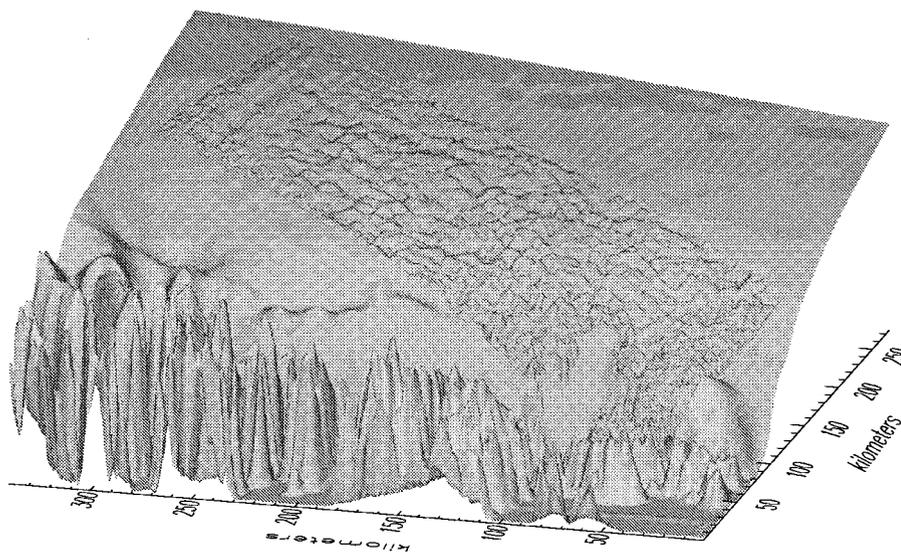
Figure 14. Shaded surface showing the combination of radar-altimetry-derived digital elevation model (DEM) and the smoother interferometry-derived DEM on Greenland's west coast [from *Joughin et al.*, 1996b]. Reprinted from the *Journal of Glaciology* with permission of the International Glaciological Society.
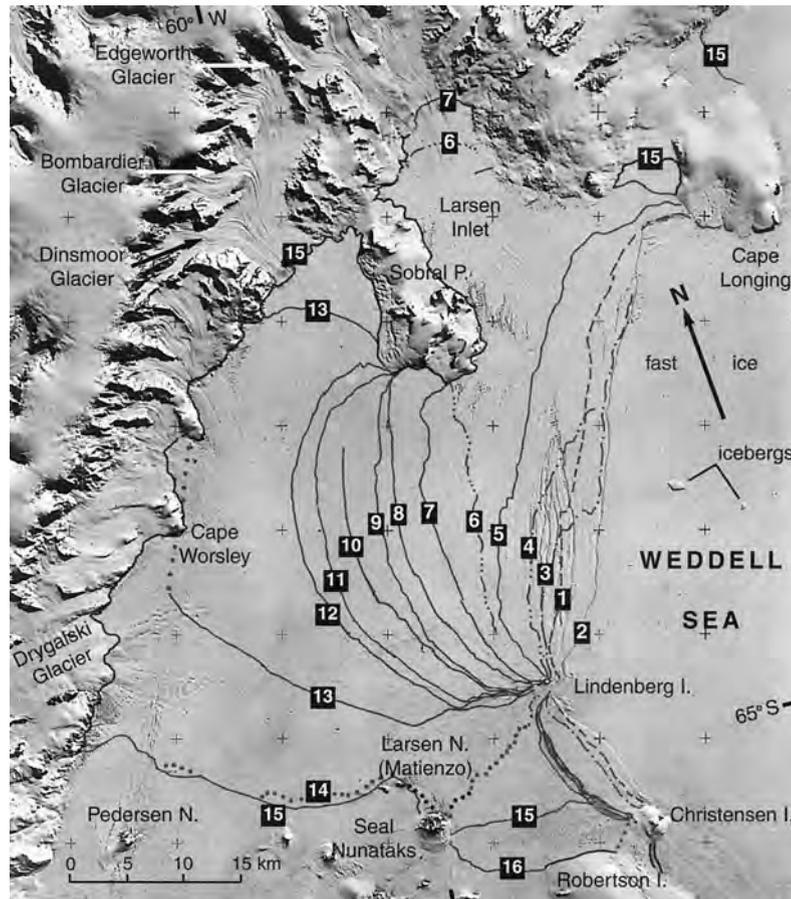
Figure 15. Section of the Kosmos KATE-200 photograph taken on October 3, 1975, showing superimposed the ice front positions (numbers in black boxes) in different years for Larsen Inlet and Larsen A ice shelf at the Antarctic Peninsula: 1, August 1963; 2, October 1975; 3, November 1978; 4, February 1979; 5, March 1986; 6, November 1989; 7, December 1992; 8, January 1993; 9, February 1993; 10, October 1994; 11, January 1995; 12, January 1995; 13, January 1995; 14, March 1995; 15, March 1997; and 16, July 1997. The front positions after 1992 were derived from ERS SAR, except for position 10, surveyed with GPS. The positions prior to 1992 correspond to Landsat TM (5 and 6), Landsat MSS (3 and 4), Argon (1), and Kosmos KATE-200 (2). [From *Skvarca et al.*, 1999]. Reprinted with permission from *Polar Research*.

using Landsat data from the 1970s until today [*Ferrigno et al.*, 1998; *Williams et al.*, 1995; *Swithinbank et al.*, 1997]. Also, Landsat TM image maps, mosaicked from many cloud-free enhanced images, are produced for some areas [*Ferrigno et al.*, 1994]. Many other studies analyzed glacier changes and fluctuations in Antarctica using SAR and visible satellite imagery from different years [*Pattyn and Decleir*, 1993; *Skvarca*, 1994; *Skvarca et al.*, 1995; *Wendler et al.*, 1996; R. Bindschadler et al., Glaciological applications with Landsat 7 imagery: Early assessments, submitted to *Remote Sensing of the Environment*, 2000]. *Hall et al.* [1992b] do the same for glaciers in Iceland and Austria, *Hall et al.* [1995d] analyzed changes for Alaskan glaciers, and *Jacobs et al.* [1997] analyzed changes for Canadian glaciers. Starting with declassified imagery from the 1960s, *Sohn et al.* [1998] study a time series of images to study fluctuations of Jacobshavn glacier in Greenland. *Skvarca et al.* [1999] summarize the retreat of ice shelves at the Antarctic

Peninsula, presenting a 30-year-long time series from various satellite sensors (Figure 15).

A cloud-free AVHRR map of Antarctica has been published by the U.S. Geological Survey [*Ferrigno et al.*, 1996]. This map was mosaicked from 38 images collected between 1980 and 1994. Details on the processing and geometric corrections are given by *Merson* [1989]. This map was used by J.-G. Winther et al. (Blue-ice areas in Antarctica derived by NOAA AVHRR satellite data, submitted to *Journal of Glaciology*, 2000) for mapping blue-ice areas.

The whole Antarctic continent has also been mapped with SAR images during the RADARSAT Antarctic Mapping Mission in fall 1997 [*Choi*, 1999]. RADARSAT was rotated from the normally right looking mode into left looking mode to allow complete coverage of Antarctica, collecting more than 8000 images in an 18-day period. Two further Antarctic mapping missions are tentatively planned for late 2000 and 2001, this time,

however, without rotating RADARSAT and therefore without coverage south of 80°S latitude. Additional information on mapping of ice sheets and the observed features is given by *Bindschadler* [1998].

4. SUMMARY

Over the last few decades the use of satellite remotely sensed data has revolutionized the field of glaciology. Remote sensing allows us to conduct research on remote areas that otherwise are hard to access and to gather data in a spatial extent not possible by fieldwork alone. Among the properties that can be measured are surface albedo, snow cover, snow depth, snow grain size, snow water equivalent, surface temperature, glacier facies, glacier velocities, glacier extent, and ice sheet topography. These measurements are used in studies on local to global scales, covering the full range from process-oriented research studies through monitoring to operational use. Normally, ground truth data are still crucial for precise interpretation of remotely sensed data.

The success of measuring a specific property from satellite is closely linked to the development of new technologies and satellite sensors. The biggest advance in remote sensing in the last decade, not only regarding snow and glacier ice studies, has been the successful introduction of satellite SAR sensors. These provide high-resolution images unaffected by cloud cover and have resulted in new techniques, such as SAR interferometry, which was unknown only 10 years ago. The potential of SAR is still not fully explored, and new methods are being introduced at present, such as mapping snow or even snow depth with interferometric techniques.

Many of the methods presented above need to account for the limitations of present satellite sensors that thus introduce uncertainties. Measuring albedo from space, for example, needs methods that account for the fact that not all of the necessary wavelengths are covered by the satellite. Imaging spectrometers covering the whole spectrum will greatly improve albedo determination in the future. Similarly, new technology is already being tested on airborne platforms and suggests what future satellite remote sensing will look like. The next generation of satellite SAR sensors (ASAR, RADARSAT-2) will be single-frequency, multipolarization SAR sensors, but even further in time, SAR sensors will eventually be multipolarization, multifrequency sensors as seen on the SIR-C/X-SAR space shuttle mission. Eventually, new and more robust algorithms will be developed that do not need to rely so heavily on assumptions, empirical relationships, or external information, for example, from models.

More spaceborne sensors will become available in the future. We may also expect that specially designed instruments with improved capabilities for snow and gla-

cier studies will open up new applications of remotely sensed data not known today. Developments of new techniques and algorithms using these new sensors will become important for the glaciological community. It normally requires updated knowledge and qualifications for working with new techniques. Therefore a challenge in the coming years will be also to utilize the enormous amount of data available (also other than remotely sensed data) and synthesize these into products of high quality and appropriate for the specific task.

Finally, we conclude that in the new century the field of satellite remote sensing will challenge the glaciological community immensely to take the full advantage of this powerful and quickly advancing tool.

REFERENCES

Abdalati, W., and K. Steffen, Snowmelt on the Greenland ice sheet as derived from passive microwave satellite data, *J. Clim.*, *10*(2), 165–175, 1997.

Andersen, T., Operational snow mapping by satellites, in *Hydrological Aspects of Alpine and High Mountain Areas*, *Proceedings of the Exeter Symposium*, *July 1982, IAHS Publ. 138*, 149–154, 1982.

Armstrong, L. C., A. Chang, A. Rango, and E. Josberger, Snow depths and grain-size relationships with relevance for passive microwave studies, *Ann. Glaciol.*, *17*, 171–176, 1993.

Baghdadi, N., Y. Gauthier, and M. Bernier, Capability of multitemporal ERS-1 SAR data for wet snow mapping, *Remote Sens. Environ.*, *60*(2), 174–186, 1997.

Bamber, J. L., Ice sheet altimeter processing scheme, *Int. J. Remote Sens.*, *15*(4), 925–938, 1994a.

Bamber, J. L., A digital elevation model of the Antarctic ice sheet derived from ERS-1 altimeter data and comparison with terrestrial measurements, *Ann. Glaciol.*, *20*, 48–54, 1994b.

Bamber, J. L., and C. R. Bentley, A comparison of satellite-altimetry and ice-thickness measurements of the Ross Ice Shelf, Antarctica, *Ann. Glaciol.*, *20*, 357–364, 1994.

Bamber, J. L., and A. R. Harris, The atmospheric correction for satellite infrared radiometer data in polar regions, *Geophys. Res. Lett.*, *21*(19), 2111–2114, 1994.

Bamber, J. L., S. Ekholm, and W. Krabill, The accuracy of satellite radar altimeter data over the Greenland ice sheet determined from airborne laser data, *Geophys. Res. Lett.*, *25*(16), 3177–3180, 1998.

Basist, A., D. Garrett, R. Ferraro, N. Grody, and K. Mitchell, A comparison between snow cover products derived from visible and microwave satellite observations, *J. Appl. Meteorol.*, *35*(2), 163–177, 1996.

Benson, C. S., Stratigraphic studies in the snow and firn of the

Greenland ice sheet, *SIPRE Res. Rep. 70*, Snow, Ice and Permafrost Res. Establ., Hanover, N. H., 1996.

Bernier, P. Y., Microwave remote sensing of snowpack properties: Potential and limitations, *Nord. Hydrol.*, *18*, 1–20, 1987.

Bindschadler, R., Monitoring ice sheet behavior from space, *Rev. Geophys.*, *36*(1), 79–104, 1998.

Bindschadler, R., and P. Vornberger, Interpretation of SAR imagery of the Greenland ice sheet using coregistered TM imagery, *Remote Sens. Environ.*, *42*(3), 162–175, 1992.

Bindschadler, R., H. J. Zwally, J. A. Major, and A. C. Brenner, Surface topography of the Greenland ice sheet from satellite radar altimetry, *NASA SP-503*, 105 pp., NASA Sci. and Tech. Inf. Div., Washington, D. C., 1989.

Bindschadler, R. A., M. A. Fahnestock, P. Skvarca, and T. A. Scambos, Surface-velocity field of the northern Larsen Ice Shelf, Antarctica, *Ann. Glaciol.*, *20*, 319–326, 1994.

Bindschadler, R., P. Vornberger, D. Blankenship, T. Scambos, and R. Jacobel, Surface velocity and mass balance of Ice Stream D and E, West Antarctica, *J. Glaciol.*, *42*(142), 461–475, 1996.

Bourdelles, B., and M. Fily, Snow grain-size determination from Landsat imagery over Terre Adélie, Antarctica, *Ann. Glaciol.*, *17*, 86–92, 1993.

Bunting, J. T., and R. P. d'Entremont, Improved cloud detection utilizing Defense Meteorological Satellite Program near infrared measurements, *Environ. Res. Pap. 765*, *Rep. AFGL-TR-82-0027*, 91 pp., Air Force Geophys. Lab., Hanscom Air Force Base, Mass., 1982.

Chang, A. T. C., J. L. Foster, and D. K. Hall, Nimbus-7 SMMR derived global snow cover parameters, *Ann. Glaciol.*, *9*, 39–44, 1987.

Chang, A. T. C., J. L. Foster, and D. K. Hall, Satellite sensor estimates of Northern Hemispheric snow volume, *Int. J. Remote Sens.*, *11*(1), 167–171, 1990.

Choi, E. M., The Radarsat Antarctic Mapping Mission, *IEEE Aerosp. Electron. Syst. Mag.*, *14*(5), 3–5, 1999.

Choudhury, B. J., and A. T. C. Chang, Two-stream theory of reflectance of snow, *IEEE Trans. Geosci. Remote Sens.*, *17*(3), 63–68, 1979.

Cline, D. W., R. C. Bales, and J. Dozier, Estimating the spatial distribution of snow in mountain basins using remote sensing and energy balance modeling, *Water Resour. Res.*, *34*(5), 1275–1285, 1998.

Davis, C. H., Comparison of ice-sheet satellite altimeter retracking algorithms, *IEEE Trans. Geosci. Remote Sens.*, *34*(1), 229–236, 1996.

Dowdeswell, J. A., and M. Williams, Surge-type glaciers in the Russian High Arctic identified from digital satellite imagery, *J. Glaciol.*, *43*(145), 489–494, 1997.

Dowdeswell, J. A., A. F. Glazovsky, and Y. Y. Macheret, Ice divides and drainage basins on the ice caps of Franz Josef-Land, Russian High Arctic, defined from Landsat, KFA-1000, and ERS-1 SAR satellite imagery, *Arct. Alp. Res.*, *27*(3), 264–270, 1995.

Dozier, J., Snow reflectance from Landsat-4 Thematic Mapper, *IEEE Trans. Geosci. Remote Sens.*, *22*(3), 323–328, 1984.

Dozier, J., Spectral signature of alpine snow cover from the Landsat Thematic Mapper, *Remote Sens. Environ.*, *28*, 9–22, 1989.

Dozier, J., and S. G. Warren, Effect of viewing angle on the infrared brightness temperature of snow, *Water Resour. Res.*, *18*(5), 1424–1434, 1982.

Dozier, J., S. R. Schneider, and D. F. McGinnis Jr., Effect of grain size and snowpack water equivalence on visible and near-infrared satellite observations of snow, *Water Resour. Res.*, *17*(4), 1213–1221, 1981.

Ekholm, S., R. Forsberg, and J. M. Brozena, Accuracy of satellite altimeter elevations over the Greenland ice sheet, *J. Geophys. Res.*, *100*(C2), 2687–2696, 1995.

Engeset, R., Change detection and monitoring of glaciers and snow using satellite microwave imaging, Ph.D. thesis, Univ. of Oslo, Oslo, 2000.

Engeset, R. V., and D. J. Weydahl, Analysis of glaciers and geomorphology on Svalbard using multitemporal ERS-1 SAR images, *IEEE Trans. Geosci. Remote Sens.*, *36*(6), 1879–1887, 1998.

Fahnestock, M., R. Bindschadler, R. Kwok, and K. Jezek, Greenland ice sheet surface properties and ice dynamics from ERS-1 SAR imagery, *Science*, *262*(5139), 1530–1534, 1993.

Fatland, D. R., and C. S. Lingle, Analysis of the 1993–1995 Bering Glacier (Alaska) surge using differential SAR interferometry, *J. Glaciol.*, *44*(148), 532–546, 1998.

Ferrigno, J. G., J. L. Mullins, J. A. Stapleton, R. A. Bindschadler, T. A. Scambos, L. B. Bellisime, J.-A. Bowell, and A. V. Acosta, Landsat TM image maps of the Shirase and Siple coast ice streams, West Antarctica, *Ann. Glaciol.*, *20*, 407–412, 1994.

Ferrigno, J. G., J. L. Mullins, J. A. Stapleton, P. S. Chavez Jr., M. G. Velasco, R. S. Williams Jr., G. F. Delinski Jr., and D. Lear, Satellite image map of Antarctica, *U.S. Geol. Surv. Misc. Invest. Ser. Map I-2560*, U.S. Geol. Surv. Inf. Serv., Denver, Colo., 1996.

Ferrigno, J. G., R. S. Williams Jr., E. Rosanova, B. K. Lucchitta, and C. Swithinbanks, Analysis of coastal change in Marie Byrd Land and Ellsworth Land, West Antarctica, using Landsat imagery, *Ann. Glaciol.*, *27*, 33–40, 1998.

Fily, M., B. Bourdelles, J. P. Dedieu, and C. Sergent, Comparison of in situ and Landsat thematic mapper derived snow grain characteristics in the Alps, *Remote Sens. Environ.*, *59*(3), 452–460, 1997.

Fily, M., J. P. Dedieu, and Y. Durand, Comparison between the results of a snow metamorphism model and remote sensing derived snow parameters in the Alps, *Remote Sens. Environ.*, *68*(3), 254–263, 1999.

Forster, R. R., B. L. Isacks, and S. B. Das, Shuttle imaging radar (SIR-C/X-SAR) reveals near-surface properties of the South Patagonian ice field, *J. Geophys. Res.*, *101*(E10), 23,169–23,180, 1996.

Foster, J. L., D. K. Hall, and A. T. C. Chang, Remote sensing of snow, *Eos Trans. AGU*, *68*(32), 682–684, Aug. 11, 1987.

Foster, J. L., A. T. C. Chang, and D. K. Hall, Comparison of snow mass estimates from prototype passive microwave snow algorithm, a revised algorithm and a snow depth climatology, *Remote Sens. Environ.*, *62*(2), 132–142, 1997.

Frezzotti, M., A. Capra, and L. Vittuari, Comparison between glacier ice velocities inferred from GPS and sequential satellite images, *Ann. Glaciol.*, *27*, 54–60, 1998.

Goldstein, R. M., H. Engelhart, B. Kamb, and R. M. Frolich, Satellite radar interferometry for monitoring ice sheet motion: Application to an Antarctic ice stream, *Science*, *262*(5139), 1525–1539, 1993.

Goodison, B. E., and A. E. Walker, Canadian development and use of snow cover information from passive microwave satellite data, in *Passive Microwave Remote Sensing of Land-Atmosphere Interactions*, *Proceedings of the ESA/NASA International Workshop*, edited by B. J. Choudhury et al., pp. 245–262, VSP, Zeist, Netherlands, 1995.

Grody, N. C., and A. N. Basist, Global identification of snow cover using SSM/I measurements, *IEEE Trans. Geosci. Remote Sens.*, *34*(1), 237–249, 1996.

Guneriussen, T., Snow characteristics in mountainous areas as observed with synthetic aperture radar (SAR) instruments, Ph.D. thesis, Univ. of Tromsø, Tromsø, Norway, 1998.

Guneriussen, T., H. Johnsen, and K. Sand, DEM corrected

ERS-1 SAR data for snow monitoring, *Int. J. Remote Sens.*, *17*(1), 181–195, 1996.

Guneriussen, T., K. A. Høgda, H. Johnson, and I. Lauknes, InSAR for estimation of changes in snow water equivalent of dry snow, in *Proceedings of the International Geoscience and Remote Sensing Symposium* (*IGARSS'00*), pp. 463–466, Inst. of Electr. and Electron. Eng., New York, 2000.

Haefliger, M., K. Steffen, and C. Fowler, AVHRR surface temperature and narrow-band albedo comparison with ground measurements for the Greenland ice sheet, *Ann. Glaciol.*, *17*, 49–54, 1993.

Haefner, H., F. Holecz, E. Meier, D. Nüesch, and J. Piesbergen, Capabilities and limitations of ERS-1 SAR data for snow cover determination in mountainous regions, in *Space at Service of Our Environment*, *Proceedings of the Second ERS-1 Symposium*, *11–14 October 1993*, *Hamburg Germany*, vol. 2, *ESA SP-361*, pp. 971–976, Eur. Space Agency, Paris, 1994.

Hall, D. K., and J. Martinec, *Remote Sensing of Ice and Snow*, 189 pp., Chapman and Hall, New York, 1985.

Hall, D. K., A. T. C. Chang, and J. L. Foster, Detection of the depth-hoar layer in the snowpack of the Arctic coastal plain of Alaska, U.S.A., using satellite data, *J. Glaciol.*, *32*(110), 87–94, 1986.

Hall, D. K., J. P. Ormsby, R. A. Bindschadler, and H. Siddalingaiah, Characterization of snow and ice reflectance zones on glaciers using Landsat Thematic Mapper data, *Ann. Glaciol.*, *9*, 1–5, 1987.

Hall, D. K., A. T. C. Chang, J. L. Foster, C. S. Benson, and W. M. Kovalick, Comparison of in situ and Landsat derived reflectance of Alaskan glaciers, *Remote Sens. Environ.*, *28*, 23–31, 1989.

Hall, D. K., W. M. Kovalick, and A. T. C. Chang, Satellite-derived reflectance of snow-covered surfaces in northern Minnesota, *Remote Sens. Environ.*, *33*(2), 87–96, 1990a.

Hall, D. K., R. A. Bindschadler, J. L. Foster, A. T. Chang, and H. Siddalingaiah, Comparison of in situ and satellite-derived reflectance of Forbindels glacier, Greenland, *Int. J. Remote Sens.*, *11*(3), 493–504, 1990b.

Hall, D. K., J. L. Foster, and A. T. C. Chang, Reflectance of snow as measured in situ and from space in sub-arctic areas in Canada and Alaska, *IEEE Trans. Geosci. Remote Sens.*, *30*(3), 634–637, 1992a.

Hall, D. K., R. S. Williams Jr., and K. J. Bayr, Glacier recession in Iceland and Austria, *Eos Trans. AGU*, *73*(12), 129, 1992b.

Hall, D. K., G. A. Riggs, and V. V. Salomonson, Development of methods for mapping global snow cover using moderate resolution imaging spectroradiometer data, *Remote Sens. Environ.*, *54*(2), 127–140, 1995a.

Hall, D. K., J. L. Foster, J. Y. L. Chien, and G. A. Riggs, Determination of actual snow covered area using Landsat TM and digital elevation model data in Glacier National Park, Montana, *Polar Rec.*, *31*(177), 191–198, 1995b.

Hall, D. K., R. S. Williams Jr., and O. Sigurdsson, Glaciological observations of Brúarjökull, Iceland, using synthetic aperture radar and thematic mapper satellite data, *Ann. Glaciol.*, *21*, 271–276, 1995c.

Hall, D. K., C. S. Benson, and W. O. Field, Changes of glaciers in Glacier Bay, Alaska, using ground and satellite measurements, *Phys. Geogr.*, *16*(1), 27–41, 1995d.

Hall, D. K., A. B. Tait, J. L. Foster, A. T. C. Chang, and M. Allen, Intercomparison of satellite-derived snow-cover maps, *Ann. Glaciol.*, in press, 2000.

Hambrey, M. J., and J. A. Dowdeswell, Flow regime of the Lambert Glacier–Amery Ice Shelf system, Antarctica: Structural evidence from Landsat imagery, *Ann. Glaciol.*, *20*, 401–406, 1994.

Herzfeld, U. C., and M. S. Matassa, An atlas of Antarctica

north of 72.1°S from Geosat radar altimeter data, *Int. J. Remote Sens.*, *20*(2), 241–258, 1999.

Herzfeld, U. C., C. S. Lingle, C. Freeman, C. A. Higginson, M. P. Lambert, L.-H. Lee, and V. A. Voronina, Monitoring changes of ice streams using time series of satellite-altimetry-based digital terrain models, *Math. Geol.*, *29*(7), 859–890, 1997.

Jacobs, J. D., E. L. Simms, and A. Simms, Recession of the southern part of Barnes Ice Cap, Baffin Island, Canada, between 1961 and 1993, determined from digital mapping of Landsat TM, *J. Glaciol.*, *43*(143), 98–102, 1997.

Jezek, K. C., M. R. Drinkwater, J. P. Crawford, R. Bindschadler, and R. Kwok, Analysis of synthetic aperture radar data collected over the southwestern Greenland ice sheet, *J. Glaciol.*, *39*(131), 119–132, 1993.

Joughin, I., R. Kwok, and M. Fahnestock, Estimation of ice-sheet motion using satellite radar interferometry: Method and error analysis with application to Humboldt Glacier, Greenland, *J. Glaciol.*, *42*(142), 564–575, 1996a.

Joughin, I., D. Winebrenner, M. Fahnestock, R. Kwok, and W. Krabill, Measurement of ice-sheet topography using satellite-radar interferometry, *J. Glaciol.*, *42*(140), 10–22, 1996b.

Joughin, I. R., R. Kwok, and M. A. Fahnestock, Interferometric estimation of three-dimensional ice-flow using ascending and descending passes, *IEEE Trans. Geosci. Remote Sens.*, *36*(1), 25–37, 1998.

Key, J., and M. Haefliger, Arctic ice surface temperature retrieval from AVHRR thermal channels, *J. Geophys. Res.*, *97*(D5), 5885–5893, 1992.

Key, J. R., J. B. Collins, C. Fowler, and R. S. Stone, High-latitude surface temperature estimates from thermal satellite data, *Remote Sens. Environ.*, *61*(2), 302–309, 1997.

Klein, A. G., D. K. Hall, and G. A. Riggs, Improving snow cover mapping in forests through the use of a canopy reflectance model, *Hydrol. Process.*, *12*, 1723–1744, 1998.

Knap, W. H., and J. Oerlemans, The surface albedo of the Greenland ice sheet: Satellite-derived and in situ measurements in the Sondre Stromfjord area during the 1991 melt season, *J. Glaciol.*, *42*(141), 364–374, 1996.

Knap, W. H., and C. H. Reijmer, Anisotropy of the reflected radiation field over melting glacier ice: Measurements in Landsat TM bands 2 and 4, *Remote Sens. Environ.*, *65*, 93–104, 1998.

Knap, W. H., C. H. Reijmer, and J. Oerlemans, Narrowband to broadband conversion of Landsat TM glacier albedos, *Int. J. Remote Sens.*, *20*(10), 2091–2110, 1999.

Koskinen, J. T., J. T. Pulliainen, and M. T. Hallikainen, The use of ERS-1 SAR data in snow melt monitoring, *IEEE Trans. Geosci. Remote Sens.*, *35*(3), 601–610, 1997.

Kyle, H. L., R. J. Curran, W. L. Barnes, and D. Escoe, A cloud physics radiometer, in *Third Conference on Atmospheric Radiation*, *Davis*, *CA*, pp. 107–109, Am. Meteorol. Soc., Boston, Mass., 1978.

Lefauconnier, B., J. O. Hagen, and J. P. Rudant, Flow speed and calving rate of Kongsbreen glacier Svalbard, using Spot images, *Polar Res.*, *13*(1), 59–65, 1994.

Legrésy, B., and F. Rémy, Altimetric observations of surface characteristics of the Antarctic ice sheet, *J. Glaciol.*, *43*(144), 265–275, 1997.

Legrésy, B., and F. Rémy, Using the temporal variability of satellite radar altimetric observations to map surface properties of the Antarctic ice sheet, *J. Glaciol.*, *44*(147), 197–206, 1998.

Li, Z. Q., and H. G. Leighton, Narrow-band to broad-band conversion with autocorrelated reflectance measurements, *J. Appl. Meteorol.*, *31*(5), 421–432, 1992.

Lingle, C. S., and D. N. Covey, Elevation changes on the East Antarctic ice sheet, 1978–1993, from satellite radar altim-

etry: A preliminary assessment, *Ann. Glaciol.*, *27*, 7–18, 1998.

Lucchitta, B. K., K. F. Mullins, A. L. Allison, and J. G. Ferrigno, Antarctic glacier tongue velocities from Landsat images: First results, *Ann. Glaciol.*, *17*, 356–366, 1993.

Lucchitta, B. K., C. E. Rosanova, and K. F. Mullins, Velocities of Pine Island Glacier, West Antarctica, from ERS-1 SAR images, *Ann. Glaciol.*, *21*, 277–283, 1995.

Markham, B. L., and J. L. Barker, Landsat MSS and TM post-calibration dynamic ranges, exoatmospheric reflectances and at-satellite temperatures, *EOSAT Landsat Tech. Not.*, *1*, 3–8, 1986.

Marshall, G. J., W. G. Rees, and J. A. Dowdeswell, The discrimination of glacier facies using multi-temporal ERS-1 SAR data, in *Sensors and Environmental Applications of Remote Sensing*, edited by J. Askne, pp. 263–269, A. A. Balkema, Brookfield, Vt., 1995.

Massom, R., *Satellite Remote Sensing of Polar Regions*, 307 pp., Lewis, Boca Raton, Fla., 1991.

Massom, R., Satellite remote sensing of polar snow and ice: Present status and future directions, *Polar Rec.*, *31*(177), 99–114, 1995.

Mattar, K. E., P. W. Vachon, D. Geudtner, A. L. Gray, I. G. Cumming, and M. Brugman, Validation of Alpine glacier velocity measurements using ERS tandem-mission SAR data, *IEEE Trans. Geosci. Remote Sens.*, *36*(3), 974–984, 1998.

Mätzler, C., and R. Hüppi, Review of signature studies for microwave remote sensing of snowpacks, *Adv. Space Res.*, *9*(1), 253–265, 1989.

McIntyre, N., Mapping ice sheets with the altimeter, *Int. J. Remote Sens.*, *12*(8), 1775–1793, 1991.

McNamara, J. P., D. L. Kane, and L. D. Hinzman, An analysis of streamflow hydrology in the Kuparuk River basin, Arctic Alaska: A nested watershed approach, *J. Hydrol.*, *206*(1–2), 39–57, 1998.

Merson, R. H., An AVHRR mosaic image of Antarctica, *Int. J. Remote Sens.*, *10*(4–5), 669–674, 1989.

Mote, T. L., M. R. Anderson, K. C. Kuivinen, and C. M. Rowe, Passive microwave-derived spatial and temporal variations of summer melt on the Greenland ice sheet, *Ann. Glaciol.*, *17*, 233–238, 1993.

Nolin, A. W., and J. Dozier, Estimating snow grain size using AVIRIS data, *Remote Sens. Environ.*, *44*(2–3), 231–238, 1993.

Nolin, A. W., J. Dozier, and L. A. K. Mertes, Mapping alpine snow using a spectral mixture modeling technique, *Ann. Glaciol.*, *17*, 121–124, 1993.

Orheim, O., and B. K. Lucchitta, Snow and ice studies by thematic mapper and multispectral scanner images, *Ann. Glaciol.*, *9*, 109–118, 1987.

Orheim, O., and B. K. Lucchitta, Numerical analysis of Landsat Thematic Mapper images of Antarctica: Surface temperatures and physical properties, *Ann. Glaciol.*, *11*, 109–120, 1988.

Parrot, J. F., N. Lyberis, B. Lefauconnier, and G. Manby, SPOT multispectral data and digital terrain model for the analysis of ice-snow fields on Antarctic glaciers, *Int. J. Remote Sens.*, *14*(3), 425–440, 1993.

Partington, K. C., Discrimination of glacier facies using multitemporal SAR data, *J. Glaciol.*, *44*(146), 42–53, 1998.

Partington, K. C., J. K. Ridley, C. G. Rapley, and H. J. Zwally, Observations of the surface properties of the ice sheets by satellite radar altimetry, *J. Glaciol.*, *35*(120), 267–275, 1989.

Paterson, W. S. B., *The Physics of Glaciers*, 480 pp., 3rd ed., Pergamon, Tarrytown, N. Y., 1994.

Pattyn, F., and H. Decleir, Satellite monitoring of ice and snow conditions in the Sør Rondane Mountains, Antarctica, *Ann. Glaciol.*, *17*, 41–48, 1993.

Phillips, H. A., I. Allison, R. Coleman, G. Hyland, P. J. Morgan, and N. W. Young, Comparison of ERS satellite radar altimeter heights with GPS-derived heights on the Amery Ice Shelf, East Antarctica, *Ann. Glaciol.*, *27*, 19–24, 1998.

Ramsay, B. H., The interactive multisensor snow and ice mapping system, *Hydrol. Process.*, *12*, 1537–1546, 1998.

Rees, W. G., J. A. Dowdeswell, and A. D. Diament, Analysis of ERS-1 synthetic aperture radar from Nordaustlandet, Svalbard, *Int. J. Remote Sens.*, *16*(5), 905–924, 1995.

Ridley, J. K., and K. C. Partington, A model of satellite radar altimeter return from ice sheets, *Int. J. Remote Sens.*, *9*(4), 601–624, 1988.

Rignot, E., Tidal motion, ice velocity and melt rate of Petermann Gletscher, Greenland, measured from radar interferometry, *J. Glaciol.*, *42*(142), 476–485, 1996.

Rignot, E., Radar interferometry detection of hinge-line migration on Ruthford Ice Stream and Carlson Inlet, Antarctica, *Ann. Glaciol.*, *27*, 25–32, 1998.

Rignot, E., R. Forster, and B. Isacks, Interferometric radar observations of Glaciar San Rafael, Chile, *J. Glaciol.*, *42*(141), 279–291, 1996.

Robinson, D. A., Hemispheric snow cover from satellites, *Ann. Glaciol.*, *17*, 367–371, 1993.

Robinson, D. A., K. F. Dewey, and R. R. Heim Jr., Global snow cover monitoring: An update, *Bull. Am. Meteorol. Soc.*, *74*(9), 1689–1696, 1993.

Rolstad, C., J. Amlien, J. O. Hagen, and B. Lundén, Visible and near-infrared digital images for determination of ice velocities and surface elevation during a surge on Osbornebreen, a tidewater glacier in Svalbard, *Ann. Glaciol.*, *24*, 255–261, 1997.

Rosanova, C. E., B. K. Lucchitta, and J. G. Ferrigno, Velocities of Thwaites Glacier and smaller glaciers along the Marie Byrd Land coast, West Antarctica, *Ann. Glaciol.*, *27*, 47–53, 1998.

Rosenthal, W., and J. Dozier, Automated mapping of montane snow cover at subpixel resolution from the Landsat Thematic Mapper, *Water Resour. Res.*, *32*(1), 115–130, 1996.

Rott, H., Remote sensing of snow, in *Proceedings of the Vancouver Symposium Large Scale Effects of Seasonal Snow Cover*, *August 1987*, *IAHS Publ. 166*, 279–290, 1987.

Rott, H., and G. Markl, Improved snow and glacier monitoring by the Landsat Thematic Mapper, in *Proceedings of a Workshop on Earthnet Pilot Project on Landsat TM Applications*, *Frascati, Italy, Dec. 1987*, *Rep. ESA SP-1102*, pp. 3–12, Eur. Space Agency, Paris, 1989.

Rott, H., and T. Nagler, Snow and glacier investigations by ERS-1 SAR—First results, in *Proceedings of the First ERS-1 Symposium—Space at the Service of Our Environment*, *Cannes, France, 4–6 November 1992*, *Rep. ESA SP-359*, pp. 577–582, Eur. Space Agency, Paris, 1993.

Rott, H., and T. Nagler, Capabilities of ERS-1 SAR for snow and glacier monitoring in alpine areas, in *Proceedings of the Second ERS-1 Symposium—Space at the Service of Our Environment*, *Hamburg, Germany, 11–14 October 1993*, *Rep. ESA SP-361*, pp. 965–970, Eur. Space Agency, Paris, 1994.

Salisbury, J. W., D. M. D'Aria, and A. Wald, Measurements of thermal infrared spectral reflectance of frost, snow, and ice, *J. Geophys. Res.*, *99*(B12), 24,234–24,240, 1994.

Scambos, T. A., and R. Bindschadler, Complex ice stream flow revealed by sequential satellite imagery, *Ann. Glaciol.*, *17*, 177–182, 1993.

Scambos, T. A., M. J. Dutkiewicz, J. C. Wilson, and R. A. Bindschadler, Application of image cross-correlation to the measurement of glacier velocity using satellite image data, *Remote Sens. Environ.*, *42*(3), 177–186, 1992.

Schjødt-Osmo, O., and R. Engeset, Remote sensing and snow monitoring: Application to flood forecasting, in *Operational Water Management*, *Proceedings of the European Water Re-*

sources Association Conference, 3–6 September 1997, edited by J. C. Refsgaard and E. A. Karalis, Lisbon, Portugal, 1997.

Shi, J., and J. Dozier, Measurements of snow and glacier-covered areas with single polarization SAR, *Ann. Glaciol.*, *17*, 72–76, 1993.

Shi, J., and J. Dozier, Mapping seasonal snow with SIR-C/X-SAR in mountaineous areas, *Remote Sens. Environ.*, *59*(2), 294–307, 1997.

Shi, J., J. Dozier, and R. Davis, Simulation of snow depth estimation from multi-frequency radar, in *Proceedings of the International Geoscience and Remote Sensing Symposium (IGARSS'90)*, pp. 1129–1132, Inst. of Electr. and Electron. Eng., New York, 1990.

Shi, J., J. Dozier, and H. Rott, Snow mapping in alpine regions with synthetic aperture radar, *IEEE Trans. Geosci. Remote Sens.*, *32*(1), 152–158, 1994.

Shi, J., S. Hensley, and J. Dozier, Mapping snow cover with repeat pass synthetic aperture radar, in *Proceedings of the International Geoscience and Remote Sensing Symposium (IGARSS'97)*, pp. 628–630, Inst. of Electr. and Electron. Eng., New York, 1997.

Skvarca, P., Changes and surface features of the Larsen Ice Shelf, Antarctica, derived from Landsat and Kosmos mosaics, *Ann. Glaciol.*, *20*, 6–12, 1994.

Skvarca, P., H. Rott, and T. Nagler, Satellite imagery, a base line for glacier variation study on James Ross Island, Antarctica, *Ann. Glaciol.*, *21*, 291–296, 1995.

Skvarca, P., W. Rack, H. Rott, and T. Ibarzábal y Donángelo, Climatic trend and the retreat and disintegration of ice shelves on the Antarctic Peninsula: An overview, *Polar Res.*, *18*(2), 151–157, 1999.

Smith, L. C., R. R. Forster, B. L. Isacks, and D. K. Hall, Seasonal climatic forcings on alpine glaciers revealed using orbital synthetic aperture radar, *J. Glaciol.*, *43*(145), 480–488, 1997.

Sohn, H.-G., K. C. Jezek, and C. J. van der Veen, Jakobshavn Glacier, West Greenland: Thirty years of spaceborne observations, *Geophys. Res. Lett.*, *25*(14), 2699–2702, 1998.

Stroeve, J., M. Haefliger, and K. Steffen, Surface temperature from ERS-1 ATSR infrared thermal satellite data in polar regions, *J. Appl. Meteorol.*, *35*(8), 1231–1239, 1996.

Stroeve, J., A. Nolin, and K. Steffen, Comparison of AVHRR-derived and in situ surface albedo over the Greenland ice sheet, *Remote Sens. Environ.*, *62*(3), 262–276, 1997.

Strozzi, T., U. Wegmüller, and C. Mätzler, Mapping wet snow covers with SAR interferometry, *Int. J. Remote Sens.*, *20*(12), 2395–2403, 1999.

Swithinbank, C., R. S. Williams Jr., J. G. Ferrigno, B. A. Seekins, B. K. Lucchitta, and C. E. Rosanova, Coastal-change and glaciological map of the Bakutis coast, Antarctica: 1972–1990, *Geol. Invest. Map I-2600-F*, Scale 1:1,000,000, U.S. Geol. Surv., Washington, D. C., 1997.

Tait, A. B., Estimation of snow water equivalent using passive microwave radiation data, *Remote Sens. Environ.*, *64*(3), 286–291, 1998.

Tait, A., and R. Armstrong, Evaluation of SMMR satellite-derived snow depth using ground-based measurements, *Int. J. Remote Sens.*, *17*(4), 657–665, 1996.

Tanré, D., C. Deroo, P. Duhaut, M. Herman, J. J. Morcrette, J. Perbos, and P. Y. Deschamps, Description of a computer code to simulate the satellite signal in the solar spectrum: The 55 code, *Int. J. Remote Sens.*, *11*(4), 659–668, 1990.

Unwin, B., and D. Wingham, Topography and dynamics of Austfonna, Nordaustlandet, Svalbard, from SAR interferometry, *Ann. Glaciol.*, *24*, 402–408, 1997.

Walker, A. E., and B. E. Goodison, Discrimination of a wet snow cover using passive microwave satellite data, *Ann. Glaciol.*, *17*, 307–311, 1993.

Warren, S. G., Optical properties of snow, *Rev. Geophys.*, *20*(1), 67–89, 1982.

Warren, S. G., and W. J. Wiscombe, A model for the spectral albedo of snow, II, Snow containing atmospheric aerosols, *J. Atmos. Sci.*, *37*, 2734–2745, 1980.

Weller, G., and B. Holmgren, The microclimate of the Arctic tundra, *J. Appl. Meteorol.*, *13*(8), 854–862, 1974.

Wendler, G., K. Ahlnäs, and C. S. Lingle, On Mertz and Ninnis Glaciers, East Antarctica, *J. Glaciol.*, *42*(142), 447–453, 1996.

Whillans, I. M., and Y. H. Tseng, Automatic tracking of crevasses on satellite images, *Cold Reg. Sci. Technol.*, *23*(2), 201–214, 1995.

Williams, R. S., Jr., D. K. Hall, and C. S. Benson, Analysis of glacier facies using satellite techniques, *J. Glaciol.*, *37*(125), 120–128, 1991.

Williams, R. S., Jr., J. G. Ferrigno, C. Swithinbank, B. K. Lucchitta, and B. A. Seekins, Coastal-change and glaciological maps of Antarctica, *Ann. Glaciol.*, *21*, 284–290, 1995.

Winther, J.-G., Landsat TM derived reflectance from a mountaineous watershed during the snowmelt season, *Nord. Hydrol.*, *23*, 273–290, 1992.

Winther, J.-G., Studies of snow surface characteristics by Landsat TM in Dronning Maud Land, Antarctica, *Ann. Glaciol.*, *17*, 27–34, 1993a.

Winther, J.-G., Landsat TM derived and in situ summer reflectance of glaciers in Svalbard, *Polar Res.*, *12*(1), 37–55, 1993b.

Winther, J.-G., and D. K. Hall, Satellite-derived snow coverage related to hydropower production in Norway—present and future, *Int. J. Remote Sens.*, *20*(15–16), 2991–3008, 1999.

Winther, J.-G., S. Gerland, J. B. Ørback, B. Ivanov, A. Blanco, and J. Boike, Spectral reflectance of melting snow in a high Arctic watershed on Svalbard: Some implications for optical satellite remote sensing studies, *Hydrol. Process.*, *13*(12–13), 2033–2049, 1999.

Wiscombe, W. J., and S. G. Warren, A model for the spectral albedo of snow, I, Pure snow, *J. Atmos. Sci.*, *37*, 2712–2733, 1980.

Zeng, Q., M. Cao, X. Feng, F. Liang, X. Chen, and W. Sheng, A study of spectral reflection characteristics for snow, ice and water in the north of China, in *Hydrological Applications of Remote Sensing and Remote Data Transmission: Proceedings of the Hamburg Symposium*, *IAHS Publ. 145*, 451–462, 1984.

Zwally, H. J., A. C. Brenner, J. A. Major, R. A. Bindschadler, and J. G. Marsh, Growth of the Greenland ice sheet: Measurement, *Science*, *246*, 1587–1589, 1989.

E. Isaksson, M. König, and J.-G. Winther, Norwegian Polar Institute, Polar Environmental Centre, 9269 Tromsø, Norway. (max.koenig@npolar.no)